



Gravitational Waves and Dark Matter in the Gauged Two-Higgs Doublet Model

Michael J. Ramsey-Musolf ^{1,2,3,4,*}

Van Que Tran ^{1,5,6,†} and Tzu-Chiang Yuan ^{6,‡}

¹*Tsung-Dao Lee Institute & School of Physics and Astronomy,
Shanghai Jiao Tong University, Shanghai 200240, China*

²*Shanghai Key Laboratory for Particle Physics and Cosmology,
Key Laboratory for Particle Astrophysics and Cosmology (MOE),
Shanghai Jiao Tong University, Shanghai 200240, China*

³*Amherst Center for Fundamental Interactions, Department of Physics,
University of Massachusetts, Amherst, MA 01003, USA*

⁴*Kellogg Radiation Laboratory, California Institute of Technology,
Pasadena, CA 91125, USA*

⁵*Phenikaa Institute for Advanced Study, Phenikaa
University, Yen Nghia, Ha Dong, Hanoi 100000, Vietnam*

⁶*Institute of Physics, Academia Sinica, Nangang, Taipei 11529, Taiwan*

Abstract

We investigate the possibility of a strong first-order electroweak phase transition during the early universe within the framework of the gauged two-Higgs doublet model (G2HDM) and explore its detectability through stochastic gravitational wave signals. The G2HDM introduces a dark replica of the Standard Model electroweak gauge group, inducing an accidental Z_2 symmetry which not only leads to a simple scalar potential at tree-level but also offers a compelling vectorial dark matter candidate. Using the high temperature expansion in the effective potential that manifests gauge invariance, we find a possible two-step phase transition pattern in the model with a strong first-order transition occurring in the second step at the electroweak scale temperature. Collider data from the LHC plays a crucial role in constraining the parameter space conducive to this two-step transition. Furthermore, satisfying the nucleation condition necessitates the masses of scalar bosons in the hidden sector to align with the electroweak scale, potentially probed by future collider detectors. The stochastic gravitational wave energy spectrum associated with the phase transition is computed. The results indicate that forthcoming detectors such as BBO, LISA, DECIGO, TianQin and Taiji could potentially detect the gravitational wave signals generated by the first-order phase transition. Additionally, we find that the parameter space probed by gravitational waves can also be searched for in future dark matter direct detection experiments, in particular those designed for dark matter masses in the sub-GeV range using the superfluid Helium target detectors.

* mjrm@sjtu.edu.cn, mjrm@physics.umass.edu

† vqtran@gate.sinica.edu.tw

‡ tcyuan@phys.sinica.edu.tw

I. INTRODUCTION

Unraveling the thermal history of electroweak symmetry breaking is considered a crucial task in both particle physics and cosmology. In the Standard Model (SM), EW symmetry breaking proceeds through a smooth crossover as indicated by lattice simulations [1–4]. However, a first-order electroweak phase transition (FOEWPT) can occur in many BSM theories, such as singlet scalar extensions [5–32], triplet scalar extensions [33–36], two-Higgs doublet models [37–76], supersymmetric models [77–80], left-right symmetric models [81, 82], Pati-Salam model [83], Georgi-Machacek model [36, 84], Zee-Babu model [85, 86], composite Higgs models [35, 87–93], neutrino mass models [94, 95] and hidden sector models involving scalars [96–105], *etc.* In some cases, the FOEWPT can occur in multiple steps [34, 106–115].

Apart from being of interest in its own right, the occurrence of FOEWPT fulfills one of the conditions established by Sakharov [116] for the realization of the electroweak baryogenesis mechanism [117–121] which accounts for the observed cosmological matter-antimatter asymmetry. A FOEWPT also admits a rich array of possible experimentally observable signatures. In particular, the presence of BSM physics related to a FOEWPT can have an impact on the properties of the Higgs boson and predicts the existence of new scalar particles with masses at or below the TeV scale, which may be probed by future collider experiments (see *e.g.* [122–126] and references therein). Apart from undergoing a strong FOEWPT, these new physics models often provide candidates for dark matter (DM), see *e.g.* [127–132]. Furthermore, a FOEWPT can result in the formation of bubble nucleation, which can expand and collide, producing stochastic gravitational waves (GWs) (see [133] for a brief review). This GW signal is potentially within the reach of upcoming space-based laser interferometer GW detectors, such as LISA [134, 135], BBO [136], TianQin [137, 138], Taiji [139, 140] and DECIGO [141–143].

One of the most straightforward extensions to SM involves the presence of a

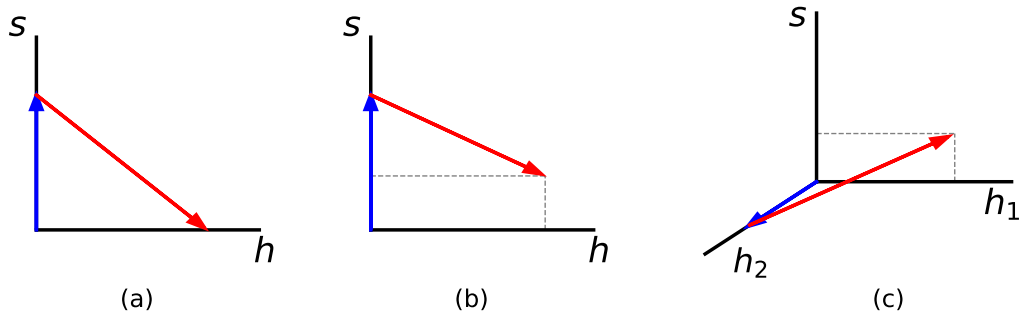


Figure 1. Patterns of a two-step transition at finite temperature. The left and center panels are for two background fields scenarios while the right panel is for three background fields scenarios. Here, $h \equiv h_1$ indicates the SM Higgs background field while s and h_2 represent new scalar boson background fields. The blue and red arrows represent the first and second step transitions, respectively. The end point of the red arrow is the electroweak vacuum value.

real singlet scalar field alongside the SM Higgs doublet field, accompanied by the imposition of a discrete Z_2 symmetry. In such the framework, it can admit a strong FOEWPT in the two-step phase transition $(0,0) \rightarrow (0,s) \rightarrow (h,0)$ as depicted in the left panel of Fig. 1 — where s (h) represents classical background field of the singlet (SM doublet) [144]¹. In the case of spontaneous Z_2 breaking [30], the inclusion of the cubic term (Th^3) in the effective potential can allow for the occurrence of a FOEWPT through $(0,0) \rightarrow (0,s) \rightarrow (h,s)$ as depicted in the center panel of Fig. 1. However, it is worth noting that the presence of this cubic term is subject to the issue of gauge dependence [145]. Nevertheless, to facilitate these transitions, the mass of the singlet scalar must be confined to be light. In particular, necessitating the occurrence of a two-step EWPT like the left panel of Fig. 1 requires

$$T_1 > T_2 \sim T_{\text{EW}} , \quad (1)$$

¹ Derived from an analysis of the high-temperature expansion of the thermal effective potential.

where $T_1(T_2)$ is the critical temperature in the first (second) step and T_{EW} is the temperature at electroweak (EW) scale. If the Z_2 symmetry is preserved at zero temperature (left panel of Fig. 1), the scalar singlet acquires its mass solely from the SM VEV. The requirement in (1) sets the scalar singlet mass to be below 700 GeV [122]. On the other hand, for the spontaneous Z_2 breaking case (center panel of Fig. 1), the scalar singlet mass is confined to below 50 GeV and the associated GW signals are typically too low to be probed by future GW detectors [30].

Furthermore, for the Z_2 symmetry preserving model, where the singlet scalar gets zero vacuum expectation value (VEV) at zero temperature, the singlet scalar can remain stable and serve as a DM candidate. This straightforward extension of SM incorporating a Z_2 symmetric potential allows us to perform gauge-invariant and scale-invariant treatments of EWPT computation. However, except for small DM mass in the range of $65 \sim 200$ GeV that can be probed by future colliders, this scenario is ruled out by direct detection experiments [144].

We thus ask following questions:

- In what context the upper limit on the new scalar mass due to the requirement of the two-step FOEWPT can be relaxed?
- Can such the model yield a DM candidate that satisfies the correct DM relic abundance and evades current DM direct detection constraints?
- Can the GW signals generated from FOEWPT detectable at forthcoming GW detectors and how does it interplay with DM direct detection signals?

In this analysis, we address these questions within the framework of a simplified G2HDM [146, 147] which is based on the original version proposed in [148]. In addition to the SM $SU(2)_L$ doublet H_1 and singlet scalars Φ_H , this model incorporates an extra inert doublet H_2 . While inert at zero temperature, this inert doublet can develop a background field (*i.e.*, VEV) at high temperature (high-T), resulting in rich phase transition patterns. Using the high-T expansion approximation

in the effective potential that manifests gauge invariance, we find a particularly novel and interesting two-step phase transition, with the first step leading to the inert doublet vacuum and the subsequent step returning to the true EW vacuum with non-zero SM doublet and singlet scalar VEVs as depicted schematically in the right panel of Fig. 1. The first-order phase transition may take place in the second step. In the second step the singlet can develop a new VEV v_Φ along with the SM VEV v from H_1 , thereby providing additional contributions to the masses of new scalars. This can lead to a relaxation of the upper bounds on masses of extra scalars in the model while archiving the two-step FOEWPT.

Moreover, the model naturally accommodates a hidden h -parity, if not spontaneously broken at zero temperature, ensuring that the lightest h -parity odd particle serves as the DM candidate. The DM candidate in the model can be either a complex scalar [149], a hidden heavy neutrino, or a non-abelian vector gauge boson — all of which are electrically neutral and possess odd h -parity. In this work, we will focus on the hidden gauge bosons $W'^{(p,m)}$ as the DM candidate [146, 147].

We demonstrate that the stochastic GW signals from the two-step FOEWPT in the simplified G2HDM can be probed in future GW experiments. The predictions of GW signals in this study are derived from the high-T expansion approximation in the one-loop effective potential, which preserves gauge invariance. To attain more accurate results and ensure a realistic perturbative treatment [145], it is imperative to incorporate a two-loop finite temperature effective potential which has yet been computed for G2HDM. Our investigation reveals that the parameter space accessible through GWs can also be explored in upcoming DM direct detection experiments. Specifically, we highlight the relevance of experiments tailored for detecting DM with masses in the sub-GeV range, utilizing superfluid Helium target detectors.

The layout of this paper is as follows. In Sec. II, we will briefly review the simplified version of G2HDM and its phenomenological constraints. In Sec. III,

after a succinct review of the current status of theoretical EWPT computation, we present our analysis in G2HDM using the high-T expansion of the finite temperature effective potential in order to maintain gauge invariance. We focus on the two-step transition pattern and identify parameter space where the desired pattern can occur. In Sec. [IV](#), we present the stochastic GW prediction signals for the FOEWPT. In Sec. [V](#), we discuss the DM direct detection probes. We conclude in Sec. [VI](#). Six appendices are compiled for [\(A\)](#) field dependent masses, [\(B\)](#) thermal masses, [\(C\)](#) thermal integrals, [\(D\)](#) gauge invariant method beyond leading order computation and scale dependence of the effective potential at finite temperature, [\(E\)](#) critical temperatures, and [\(F\)](#) renormalization group equations.

II. THE SIMPLIFIED G2HDM

In this section, we will briefly review the simplified version of G2HDM [[146](#), [147](#)]. Unlike the original G2HDM presented in [[148](#)], the simplified version has omitted the $SU(2)_H$ triplet scalar Δ_H , thereby simplifying the scalar potential. The scalar sector in the simplified G2HDM consists of the SM Higgs doublet H_1 and a second inert Higgs doublet H_2 of $SU(2)_L$, as well as a hidden doublet Φ_H of $SU(2)_H$. Regarding the two doublets H_1 and H_2 , the model is different from the popular inert Higgs doublet model (IHDM) in that they are combined into a doublet of the hidden $SU(2)_H$. Their extended electroweak quantum numbers and h -parity are summarized in [Table I](#) for reference.

We note that the model also consists of heavy hidden fermions for the cancellations of gauge and gravitational anomalies. The hidden doublet Φ_H of $SU(2)_H$ can provide realistic Yukawa couplings and mass spectra for the extra fermions and vector bosons. The loop-induced flavor changing neutral current (FCNC) processes within the model have also been investigated [[150](#), [151](#)]. Additionally, the G2HDM is capable of addressing the recent high precision measurement of the W

Scalar	$SU(2)_L$	$SU(2)_H$	$U(1)_Y$	$U(1)_X$	h -parity
$H = \begin{pmatrix} H_1 \\ H_2 \end{pmatrix}$	2	2	$\frac{1}{2}$	$\frac{1}{2}$	+
$\Phi_H = \begin{pmatrix} G_H^p \\ \Phi_H^0 \end{pmatrix}$	1	2	0	$\frac{1}{2}$	-
					+

Table I. Higgs sector in the simplified G2HDM and their quantum number assignments. Note that $H_{1,2}$ individually transform as $SU(2)_L$ doublets and together as a doublet under $SU(2)_H$, whereas the components of the $SU(2)_H$ doublet transform individually as $SU(2)_L$ singlets.

boson mass at the CDF II detector [152]. Many other phenomenological aspects of the model have been explored as well in [153–158]. A pure dark gauge-Higgs sector of $SU(2) \times U(1)$ with the dark gauge bosons $W'^{(p,m)}$ implemented as a self-interacting DM candidate was recently pursued in [159].

A. Higgs Potential and Spontaneous Symmetry Breaking

The most general Higgs potential which is invariant under the extended electroweak gauge group $SU(2)_L \times U(1)_Y \times SU(2)_H \times U(1)_X$ is given by

$$\begin{aligned}
V = & -\mu_H^2 (H^{\alpha i} H_{\alpha i}) + \lambda_H (H^{\alpha i} H_{\alpha i})^2 + \frac{1}{2} \lambda'_H \epsilon_{\alpha\beta} \epsilon^{\gamma\delta} (H^{\alpha i} H_{\gamma i}) (H^{\beta j} H_{\delta j}) \\
& -\mu_\Phi^2 \Phi_H^\dagger \Phi_H + \lambda_\Phi (\Phi_H^\dagger \Phi_H)^2 + \lambda_{H\Phi} (H^\dagger H) (\Phi_H^\dagger \Phi_H) + \lambda'_{H\Phi} (H^\dagger \Phi_H) (\Phi_H^\dagger H),
\end{aligned} \tag{2}$$

where $(\alpha, \beta, \gamma, \delta)$ and (i, j) refer to the $SU(2)_H$ and $SU(2)_L$ indices respectively, all of which run from 1 to 2, and $H^{\alpha i} = H_{\alpha i}^*$.

To study general spontaneous symmetry breaking (SSB) at finite temperature,

we parameterize the fields according to standard practice

$$H_1 = \begin{pmatrix} h_1^+ \\ H_1^0 = \frac{h_{1c} + h_{\text{SM}}}{\sqrt{2}} + i\frac{G_1^0}{\sqrt{2}} \end{pmatrix}, \quad H_2 = \begin{pmatrix} h_2^+ \\ H_2^0 = \frac{h_{2c} + h_2^0}{\sqrt{2}} + i\frac{G_2^0}{\sqrt{2}} \end{pmatrix}, \quad (3)$$

$$\Phi_H = \begin{pmatrix} G_H^p = \frac{G_H^1 + iG_H^2}{\sqrt{2}} \\ \Phi_H^0 = \frac{\phi_{Hc} + \phi_H}{\sqrt{2}} + i\frac{G_H^0}{\sqrt{2}} \end{pmatrix}, \quad (4)$$

where h_{ic} and ϕ_{Hc} are the only nonvanishing temperature dependent classical background field components in H_i and Φ_H fields respectively. The temperature dependence in the background fields is implicit.

In terms of the background fields, the effective potential at tree level is

$$V_0(h_{1c}, h_{2c}, \phi_{Hc}) = \frac{1}{4} \left[-2\mu_H^2 (h_{1c}^2 + h_{2c}^2) + \lambda_H (h_{1c}^2 + h_{2c}^2)^2 - 2\mu_{\Phi_H}^2 \phi_{Hc}^2 + \lambda_{\Phi} \phi_{Hc}^4 \right. \\ \left. + \lambda_{H\Phi} (h_{1c}^2 + h_{2c}^2) \phi_{Hc}^2 + \lambda'_{H\Phi} h_{2c}^2 \phi_{Hc}^2 \right]. \quad (5)$$

Note that in the tree level effective potential, the $h_{ic}\phi_{Hc}$ term and all the terms involving the coupling λ'_H are absent.

B. Mass spectrum and mixing at tree level

At zero temperature, the classical background fields are the constant vacuum expectation values (VEVs) *i.e.* $h_{ic}(0) = v_i$ and $\phi_{Hc}(0) = v_{\Phi}$. Since H_2 is odd under h -parity, it plays the role as the inert Higgs doublet at zero temperature, so $v_2 = 0$. With this set up, a h -parity protects the stability of DM candidate in the model [146, 147]. The scalar potential at tree level given in Eq. (5) becomes

$$V_0(v_1, 0, v_{\Phi}) = \frac{1}{4} \left[-2\mu_H^2 v_1^2 + \lambda_H v_1^4 - 2\mu_{\Phi_H}^2 v_{\Phi}^2 + \lambda_{\Phi} v_{\Phi}^4 + \lambda_{H\Phi} v_1^2 v_{\Phi}^2 \right]. \quad (6)$$

From the h -parity assignment given in Table I, we note that while there is no mixing between H_1 and H_2 , H_1 (H_2) can mix with the lower (upper) component of

Φ_H . Specifically, the neutral components h_{SM} and ϕ_H in H_1 and Φ_H , respectively, are both even under h -parity and can combine to form two observable Higgs fields, denoted as h_1 and h_2 . This mixing can be given as

$$\begin{pmatrix} h_{\text{SM}} \\ \phi_H \end{pmatrix} = \begin{pmatrix} \cos \theta_1 & \sin \theta_1 \\ -\sin \theta_1 & \cos \theta_1 \end{pmatrix} \cdot \begin{pmatrix} h_1 \\ h_2 \end{pmatrix}, \quad (7)$$

where the mixing angle θ_1 is given by

$$\tan 2\theta_1 = \frac{\lambda_{H\Phi} v v_\Phi}{\lambda_\Phi v_\Phi^2 - \lambda_H v^2}. \quad (8)$$

The masses of h_1 and h_2 are given by

$$m_{h_1, h_2}^2 = \lambda_H v^2 + \lambda_\Phi v_\Phi^2 \mp \sqrt{\lambda_H^2 v^4 + \lambda_\Phi^2 v_\Phi^4 + (\lambda_{H\Phi}^2 - 2\lambda_H \lambda_\Phi) v^2 v_\Phi^2}. \quad (9)$$

The observed Higgs boson (which we denote as h) at the LHC is either h_1 or h_2 , depending on their masses (9) determined by the underlying portal parameters in the scalar potential. Currently, the most precise determination of the Higgs boson mass is $m_h = 125.38 \pm 0.14$ GeV, as reported in Ref. [160].

Furthermore, the h -parity odd fields H_2^0 and G_H^m can mix to produce two fields: a physical dark Higgs boson denoted as D , and an unphysical Goldstone boson \tilde{G} that gets absorbed by the W'^m boson. The mixing is given by

$$\begin{pmatrix} G_H^m \\ H_2^0 \end{pmatrix} = \begin{pmatrix} \cos \theta_2 & \sin \theta_2 \\ -\sin \theta_2 & \cos \theta_2 \end{pmatrix} \cdot \begin{pmatrix} \tilde{G} \\ D \end{pmatrix}, \quad (10)$$

where the mixing angle θ_2 satisfies

$$\tan 2\theta_2 = \frac{2v v_\Phi}{v_\Phi^2 - v^2}, \quad (11)$$

and the mass of D is

$$m_D^2 = \frac{1}{2} \lambda'_{H\Phi} (v^2 + v_\Phi^2). \quad (12)$$

\tilde{G} (\tilde{G}^*) is the Goldstone field associated with the $SU(2)_H$ gauge boson W'^m (W'^p). Its mass depends on the gauge fixings [146]. In Feynman-'t Hooft gauge it has the same mass as the W'^m (W'^p). In Landau and unitary gauge, its mass is zero and infinite respectively.

The charged Higgs H^\pm , same as h_2^\pm at zero temperature, is also h -parity odd and has a mass

$$m_{H^\pm}^2 = \frac{1}{2} (\lambda'_{H\Phi} v_\Phi^2 - \lambda'_H v^2) . \quad (13)$$

We note that the quartic coupling parameters in the scalar potential that determine the masses of h -parity odd states D and H^\pm are different from those of h -parity even states h_1 and h_2 .

The $SU(2)_H$ gauge bosons $W'^{(p,m)}$ have a mass

$$m_{W'} = \frac{1}{2} g_H \sqrt{v^2 + v_\Phi^2} , \quad (14)$$

where g_H is the gauge coupling of $SU(2)_H$. $W'^{(p,m)}$ are both electrically neutral and odd under h -parity. Therefore, they could potentially serve as dark matter candidates, provided that their mass is the lightest among all odd h -parity particles.

Finally the SM Z boson mixes with the W'_3 gauge field associated with the third generator of $SU(2)_H$ and the $U(1)_X$ gauge field X (see Ref. [146, 147] for the mass matrix). This leads to three physical fields Z_i for $i = 1, 2, 3$. We will identify Z_1 with the neutral gauge boson resonance Z observed at LEP with a mass of 91.1876 GeV [161], while the other two states can be identified as the dark photon (γ') and the dark Z boson (Z') with the ordering $m_{\gamma'} < m_{Z'}$.

The fundamental parameters in the scalar potential can be expressed in terms of particle masses by performing an inversion, as demonstrated in Refs. [146, 147,

150]:

$$v_\Phi = \begin{cases} v \cot \theta_2, & \text{for } \theta_2 > 0, \\ -v \tan \theta_2, & \text{for } \theta_2 \leq 0, \end{cases} \quad (15)$$

$$\lambda_H = \frac{1}{2v^2} (m_{h_1}^2 \cos^2 \theta_1 + m_{h_2}^2 \sin^2 \theta_1), \quad (16)$$

$$\lambda_\Phi = \frac{1}{2v_\Phi^2} (m_{h_1}^2 \sin^2 \theta_1 + m_{h_2}^2 \cos^2 \theta_1), \quad (17)$$

$$\lambda_{H\Phi} = \frac{1}{2vv_\Phi} (m_{h_2}^2 - m_{h_1}^2) \sin(2\theta_1), \quad (18)$$

$$\lambda'_{H\Phi} = \frac{2m_D^2}{v^2 + v_\Phi^2}, \quad (19)$$

$$\lambda'_H = \frac{2}{v^2} \left(\frac{m_D^2 v_\Phi^2}{v^2 + v_\Phi^2} - m_{H^\pm}^2 \right). \quad (20)$$

From (14), we also obtain

$$g_H = \frac{2m_{W'}}{\sqrt{v^2 + v_\Phi^2}}. \quad (21)$$

Thus one can use m_{h_2} , $m_{W'}$, m_D , m_{H^\pm} , θ_1 and θ_2 as input in our numerical scan. The additional free parameters in the model are the heavy hidden fermion mass m_{fH} , the $U(1)_X$ gauge coupling g_X and the Stueckelberg mass m_X .

C. Constraints

The constraints on the model have been studied in [146, 147, 150], taking into account the theoretical constraints on the scalar potential, as well as constraints from Higgs measurements at the LHC, electroweak precision data, dark photon and dark matter searches. Here we summarize these constraints as follows.

Theoretical constraints:

(a) Vacuum Stability: To ensure that the scalar potential has a minimum value, we adopt the copositivity conditions suggested by [154], which provide the following set of constraints on the scalar potential parameters

$$\tilde{\lambda}_H(\eta) \geq 0, \quad \lambda_\Phi \geq 0 \quad \text{and} \quad \tilde{\lambda}_{H\Phi}(\xi) + 2\sqrt{\tilde{\lambda}_H(\eta)\lambda_\Phi} \geq 0, \quad (22)$$

where $\tilde{\lambda}_H(\eta) \equiv \lambda_H + \eta\lambda'_H$ and $\tilde{\lambda}_{H\Phi}(\xi) \equiv \lambda_{H\Phi} + \xi\lambda'_{H\Phi}$ with $0 \leq \xi \leq 1$ and $-1 \leq \eta \leq 0$.

(b) *Perturbative Unitarity*: The condition for perturbative unitarity, as presented in [146, 147, 154], provides the following constraints

$$|\lambda_H|, |\lambda_\Phi| \leq 4\pi, |\lambda_{H\Phi}| \leq 8\pi, |\lambda'_{H\Phi}|, |\lambda'_H| \leq 8\sqrt{2}\pi, \quad (23)$$

$$|2\lambda_H \pm \lambda'_H| \leq 8\pi, |\lambda_{H\Phi} + \lambda'_{H\Phi}| \leq 8\pi, \quad (24)$$

$$\left| (\lambda_H + \lambda'_H/2 + \lambda_\Phi) \pm \sqrt{2\lambda_{H\Phi}^2 + (\lambda_H + \lambda'_H/2 - \lambda_\Phi)^2} \right| \leq 8\pi, \quad (25)$$

$$\left| (5\lambda_H - \lambda'_H/2 + 3\lambda_\Phi) \pm \sqrt{(5\lambda_H - \lambda'_H/2 - 3\lambda_\Phi)^2 + 2(2\lambda_{H\Phi} + \lambda'_{H\Phi})^2} \right| \leq 8\pi. \quad (26)$$

We note that the perturbativity bound can be crucial in some BSM Higgs scenarios, such as the real triplet scalar extension model [130]. However, to impose this constraint, two-loop renormalization group equations are required. We defer to future work an evaluation of the two-loop β -functions and corresponding perturbativity constraints, keeping in mind that the latter may lead to further reductions in the viable parameter space.

Higgs data constraints: The mixing between h -parity even scalar bosons, h_1 (Higgs boson) and h_2 , results in modifications on the couplings between the Higgs boson and SM particles as compared with those in the SM. Moreover, in addition to contributions from the SM charged particles, the process $h \rightarrow \gamma\gamma$ receives contributions from hidden charged fermions f^H and charged Higgs H^\pm in the G2HDM. The analytical formulation of this 1-loop process is presented in [150]. Utilizing the Higgs signal strength data of the decays into $\gamma\gamma, \tau^+\tau^-, W^+W^-$ and ZZ from CMS measurement [162], we derive a constraint on the mixing angle, finding that $|\sin\theta_1| \lesssim 0.35$. When combining Higgs signal strength data from both CMS [162] and ATLAS [163], a more stringent limit of $|\sin\theta_1| \lesssim 0.25$ is established, which is depicted as a gray shaded area in Fig. 2.

We consider the gauge boson W' with a sub-GeV mass range as the DM candidate in the model, as studied in [146, 147]. Therefore, h_1 (identified as h here) can

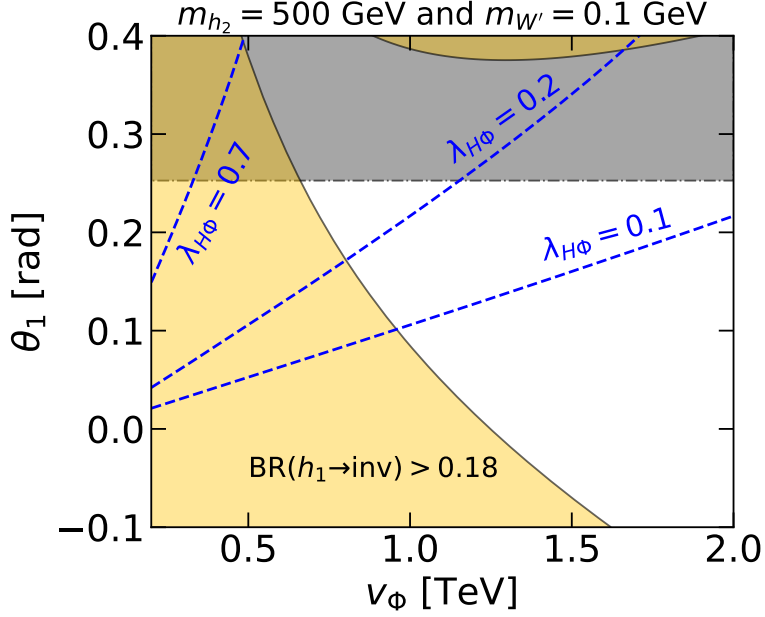


Figure 2. The collider constraints projected onto the plane of (v_Φ, θ_1) . The gray shaded region represents the exclusion region from the combined Higgs signal strength data at the LHC [162, 163], while the yellow shaded region indicates the exclusion from the branching ratio of Higgs invisible decay measurements. The blue dashed lines represent the Higgs portal parameter $\lambda_{H\Phi}$ values. The relevant parameters $m_{h_2} = 500$ GeV and $m_{W'} = 0.1$ GeV are fixed.

decay invisibly into a pair of $W'^{(p,m)}$. The invisible branching ratio can be given by

$$\text{BR}(h_1 \rightarrow \text{inv}) = \frac{\Gamma(h_1 \rightarrow W'^p W'^m)}{\Gamma_{h_1}}, \quad (27)$$

where $\Gamma_{h_1} \simeq \cos^2 \theta_1 \Gamma_h^{\text{SM}} + \Gamma(h_1 \rightarrow W'^p W'^m)$ is the total decay width of the 125.38 GeV Higgs boson, $\Gamma_h^{\text{SM}} = 4.1$ MeV is the SM decay width and $\Gamma(h_1 \rightarrow W'^p W'^m)$ is its invisible decay width. The latter is given by

$$\Gamma(h_1 \rightarrow W'^p W'^m) = \frac{g_H^4 (v \cos \theta_1 - v_\Phi \sin \theta_1)^2 m_{h_1}^3}{256\pi m_{W'}^4} \left(1 - \tau_{W'} + \frac{3}{4} \tau_{W'}^2 \right) \sqrt{1 - \tau_{W'}}, \quad (28)$$

with $\tau_{W'} = 4m_{W'}^2/m_{h_1}^2$. Recently, CMS set a limit of $\text{BR}(h_1 \rightarrow \text{inv}) < 0.18$ at 95% C.L., assuming that the Higgs boson production cross-section via vector boson fusion is comparable to the SM prediction [164]. The exclusion region from the Higgs invisible decays is shown on the (v_Φ, θ_1) plane as the yellow shaded region in Fig. 2.

Combining the constraints from the Higgs signal strengths and Higgs invisible width yields a lower bound on v_Φ and an upper bound on the Higgs portal parameter $\lambda_{H\Phi}$, as illustrated in Fig. 2. Specifically, for fixed values of $m_{h_2} = 500$ GeV and $m_{W'} = 0.1$ GeV, the collider data require $v_\Phi \gtrsim 600$ GeV and $\lambda_{H\Phi} \lesssim 0.5$.

As we will see later the Higgs portal parameter $\lambda_{H\Phi}$ can have a significant impact on the tree-level effects of the first-order electroweak phase transition. A relatively large value of $\lambda_{H\Phi}$ is required to have a substantial effect [110]. By combining this requirement with the Higgs signal strength data, an upper bound on v_Φ can be derived. For instance, our results show that if a first-order electroweak phase transition necessitates $\lambda_{H\Phi} > 0.2$, it leads to a constraint of $v_\Phi < 1.2$ TeV, as demonstrated in Fig. 2.

Electroweak precision and dark photon/ Z' measurements:

We consider constraints from electroweak precision measurements at the Z pole [161], as well as from Z' [165] and dark photon physics (see [166] for a recent review). For the specific range of light dark photon and Z' masses, *i.e.*, $m_{A',Z'} < m_Z$, considered in this study, these constraints require the new gauge couplings g_H and g_X to be less than $\sim 10^{-3}$ [146, 147]. In this analysis, we also follow Ref. [150] to take into account the recent W boson mass measurement at the CDF II [167].

DM constraints:

(a) Relic density: The main annihilation process of a (sub-)GeV DM W' is $W'^p W'^m \rightarrow f \bar{f}$ via s-channel, mediated by Z' and γ' . However, due to the smallness of the gauge couplings g_H and g_X , the cross sections of such processes are

typically suppressed except in the resonant regions where the mediator masses are approximately twice the DM mass, as discussed in [146, 147]. In fact, the annihilation process with a heavier mediator Z' near the resonance can account for the observed DM relic density, $\Omega_{\text{DM}}h^2 = 0.120 \pm 0.001$ from the Planck Collaboration [168]. Here we utilize `micrOMEGAs` package [169] to calculate the DM relic density.

(b) Direct detection: The DM W' can scatter off the target material in underground detectors resulting in a recoil energy that can be detected. The scattering cross section between the DM and the nucleon is dominated by the dark photon mediation process, as the dark photon is considered to have the lightest mass among the mediators [146, 147]. We again use `micrOMEGAs` package to calculate the DM-nucleon scattering cross section. The results of the cross section are compared against recent upper limits from experiments including CRESST III [170], DarkSide-50 [171, 172], XENON1T [173, 174], XENONnT [175], PandaX-4T [176] and LZ [177].

(c) Indirect detection and mono-jet: as shown in [146, 147], the results of electroweak precision measurements lead to a suppression of the new gauge couplings, resulting in a small DM annihilation cross section that easily satisfies the canonical limits set for various channels by Fermi-LAT data [178, 179]. Furthermore, this suppression of the gauge couplings also leads to a minuscule production cross section for the mono-jet signal at the LHC [146, 147]. Thus we do not include the constraints from indirect detection and mono-jet in this analysis.

III. ELECTROWEAK PHASE TRANSITION

In the literature, a common approach to calculate the EWPT is through the use of perturbation theory. However, this method becomes unreliable at temperatures $T > 0$ due to infrared (IR) bosonic contribution to thermal loops [180], which

can cause a breakdown of the theory near the phase transition. Apart from this inherent shortcoming, the reliability of $T > 0$ perturbative computations can be improved using the well-known daisy resummation [181, 182], though the convergence remains slow. Recent attempts to improve the thermal resummation have been performed in Refs. [183, 184]. Additionally, the conventional perturbative studies are often challenged by gauge dependence issues [145, 185]. Efforts in Refs. [145, 186] have been made to remove this gauge dependence which is guaranteed by the Nielsen identities [187, 188]. The choice of renormalization scheme and renormalization scale can also introduce additional uncertainties, leading to theoretical predictions that can vary significantly [189–191].

A more systematic approach to include thermal resummation is through the use of the dimensionally reduced 3d effective field theory (EFT)[192, 193]. Recently, an automated package has been developed for this [194]. The use of the dimensional reduced 3d EFT in the calculation of the EWPT has been studied in models such as the triplet model [34, 115]. Efforts have also been made to combine thermal resummation with gauge invariance using the dimensional reduced 3d EFT [74, 189, 190, 195, 196]. Another combination of thermal resummation and gauge invariance has also been developed recently [197], which uses the 4d perturbation theory with a consistent power counting. Ultimately, one must rely on non-perturbative (lattice) computations to fully include the important bosonic IR contributions. For recent studies of the EWPT using Monte Carlo simulations, see Refs. [29, 198–200]. Importantly, one requires such lattice studies to determine the parameter-space boundary between a *bona fide* phase transition and a smooth crossover. In what follows, we rely on perturbation theory to identify the potentially FOWEPT-viable regions of parameter space, and defer a complete non-perturbative study to the future.

A. One Loop Finite Temperature Effective Potential With Daisy Resummation

The finite temperature effective potential V_{eff} at one loop is given by

$$V_{\text{eff}}(h_{1c}, h_{2c}, \phi_{Hc}, T) = V_0(h_{1c}, h_{2c}, \phi_{Hc}) + V_1(h_{1c}, h_{2c}, \phi_{Hc}, T) , \quad (29)$$

where V_0 is given by Eq. (5).

The one loop correction $V_1(h_{1c}, h_{2c}, \phi_{Hc}, T)$ can be split into several pieces

$$\begin{aligned} V_1(h_{1c}, h_{2c}, \phi_{Hc}, T) &= V_{\text{CW}}(h_{1c}, h_{2c}, \phi_{Hc}) + \Delta V_1(h_{1c}, h_{2c}, \phi_{Hc}, T) \\ &\quad + \Delta V_{\text{C.T.}}(h_{1c}, h_{2c}, \phi_{Hc}) . \end{aligned} \quad (30)$$

The first term is the Coleman-Weinberg effective potential [201, 202] which is temperature independent, the second term is finite temperature correction, and the third term $\Delta V_{\text{C.T.}}$ is the counter term. The Coleman-Weinberg effective potential in $4 - \epsilon$ dimensional regularization can be expressed as

$$\begin{aligned} V_{\text{CW}}(h_{1c}, h_{2c}, \phi_{Hc}) &= \frac{1}{64\pi^2} \sum_i (-1)^{2s_i} n_i m_i^4(h_{1c}, h_{2c}, \phi_{Hc}) \\ &\quad \times \left\{ \log \left(\frac{m_i^2(h_{1c}, h_{2c}, \phi_{Hc})}{\mu^2} \right) - C_i - C_{\text{UV}} \right\} , \end{aligned} \quad (31)$$

where m_i denotes the field dependent mass (See Appendix A) of the particle i with spin $s_i = (0, 1/2, 1)$ and number of degree of freedom n_i ; $C_i = 3/2$ for scalars and fermions and $5/6$ for gauge bosons;

$$C_{\text{UV}} = \frac{2}{\epsilon} - \gamma_E + \log 4\pi , \quad (32)$$

with $\gamma_E = 0.5772\dots$ denotes the Euler-Mascheroni constant; μ is a renormalization scale (See Appendix F). The finite temperature correction piece is [106, 203]

$$\Delta V_1(h_{1c}, h_{2c}, \phi_{Hc}, T) = \frac{T^4}{2\pi^2} \sum_i (-1)^{2s_i} n_i \mathcal{J}_i \left(\frac{m_i(h_{1c}, h_{2c}, \phi_{Hc})}{T} \right) . \quad (33)$$

Here $\mathcal{J}_i(x)$ is the one loop thermal function (with daisy resummation) defined by (C7) in Appendix C. In the G2HDM, we have to sum over the following 3 sets of particles inside the loop

$$\{S_1, S_2, S_3, S_4, P_1, P_2, P_3, P_4, G^\pm, H^\pm\} , \quad (34)$$

$$\{W_L^\pm, W_T^\pm, W_L'^2, W_T'^2, Z_{1L}, Z_{2L}, Z_{3L}, Z_{4L}, Z_{1T}, Z_{2T}, Z_{3T}, Z_{4T}, \gamma_L, \gamma_T\} , \quad (35)$$

$$\{l, \nu, q, l^H, \nu^H, q^H\} . \quad (36)$$

In (34), $S_i (i = 1, 2, 3, 4)$ and $P_i (i = 1, 2, 3, 4)$ are the CP-even and CP-odd scalars respectively. In (35), $Z_i (i = 1, 2, 3, 4)$ are the mass eigenstates of the massive neutral gauge bosons. For the general mass spectra of the model, see Appendix A for details. The corresponding degrees of freedom n_i are

$$\begin{aligned} n_{S_i} &= 1, & n_{P_i} &= 1, & n_{H^\pm} &= 2, & n_{G^\pm} &= 2, \\ n_{W_L^\pm} &= 2, & n_{W_T^\pm} &= 4, & n_{W_L'^2} &= 1, & n_{W_T'^2} &= 2, & n_{Z_{iL}} &= 1, & n_{Z_{iT}} &= 2, & n_{\gamma_L} &= 1, & n_{\gamma_T} &= 2, \\ n_l &= 4, & n_\nu &= 4, & n_{l^H} &= 4, & n_{\nu^H} &= 4, & n_q &= 12, & n_{q^H} &= 12. \end{aligned}$$

We note that due to the thermal mass corrections for the scalars and the longitudinal gauge bosons, the summation in Eq. (33) has to be treated slightly different from the summation in Eq. (31) as given explicitly in (C7). This is the result of the daisy resummation [204, 205].

In order to facilitate the analysis of the phase transition, we limit our consideration to the leading terms of the thermal correction functions \mathcal{J}_B and \mathcal{J}_F for the boson B and fermion F respectively. As a result, the thermal effective potential can be expressed in this high-T expansion as follows:

$$V_{\text{eff}}^{\text{HT}}(h_{1c}, h_{2c}, \phi_{Hc}, T) = V_0(h_{1c}, h_{2c}, \phi_{Hc}) + \frac{1}{2}\Pi_{H_1}(T)h_{1c}^2 + \frac{1}{2}\Pi_{H_2}(T)h_{2c}^2 + \frac{1}{2}\Pi_{\Phi_H}(T)\phi_{Hc}^2, \quad (37)$$

where $\Pi_{H_1}(T)$, $\Pi_{H_2}(T)$ and $\Pi_{\Phi_H}(T)$ are the thermal mass corrections for the scalar fields and their formulas are provided by (B1), (B2) and (B3) respectively in Appendix B.

B. Thermal history

Given the three possible non-zero VEVs $(h_{1c}, h_{2c}, \phi_{Hc})$, there are eight combinations of possible extrema. To ensure the stability of the dark matter candidate, it is necessary that $h_{2c} = 0$ at zero temperature, thereby restoring the h -parity in the model [146, 147]. We first note that, with a high-T expansion of the effective potential given in Eq. (37), a single-step transition to the electroweak vacuum, *i.e.*, $(0, 0, 0) \rightarrow (h_{1c}, 0, \phi_{Hc})$, cannot be of first-order type. This is due to conflicting requirements that arise from the need for both h_{1c} and ϕ_{Hc} to be real and non-zero, as well as the positivity and minimum conditions of the scalar potential at zero temperature [144].

After thoroughly scanning the parameter space in the model, we find a phase transition pattern that satisfies the electroweak vacuum requirement and leads to a strong first-order phase transition, as illustrated in the right panel of Fig. 1 where $s \equiv \phi_{Hc}$, $h_1 \equiv h_{1c}$ and $h_2 \equiv h_{2c}$. This pattern involves two-steps: $(0, 0, 0) \rightarrow (0, h_{2c}, 0) \rightarrow (h_{1c}, 0, \phi_{Hc})$, where the first step is a second-order phase transition, and the second is a first-order phase transition. We note that other two-step transition patterns are possible; however, these patterns may not result in a strong first-order phase transition. For instance, for the transition patterns of $(0, 0, 0) \rightarrow (0, 0, \phi'_{Hc}) \rightarrow (h_{1c}, 0, \phi_{Hc})$ and $(0, 0, 0) \rightarrow (h'_{1c}, 0, 0) \rightarrow (h_{1c}, 0, \phi_{Hc})$, the scalar potential in Eq. (37) can be reduced to the one that is the same as in a real singlet scalar extension model with Z_2 symmetry, wherein the two-step transition ended up with two non-zero VEVs cannot generate a first-order phase transition [144]. We would like to mention that multiple-step transitions beyond two-step transitions can occur, and a first-order phase transition can arise among these steps. However, for this analysis, we have restricted ourselves to the two-step EWPT.

Fig. 3 illustrates the evolution of electroweak vacuum (left panel) and minimal of the effective potential (right panel) as functions of temperature. Here we introduce

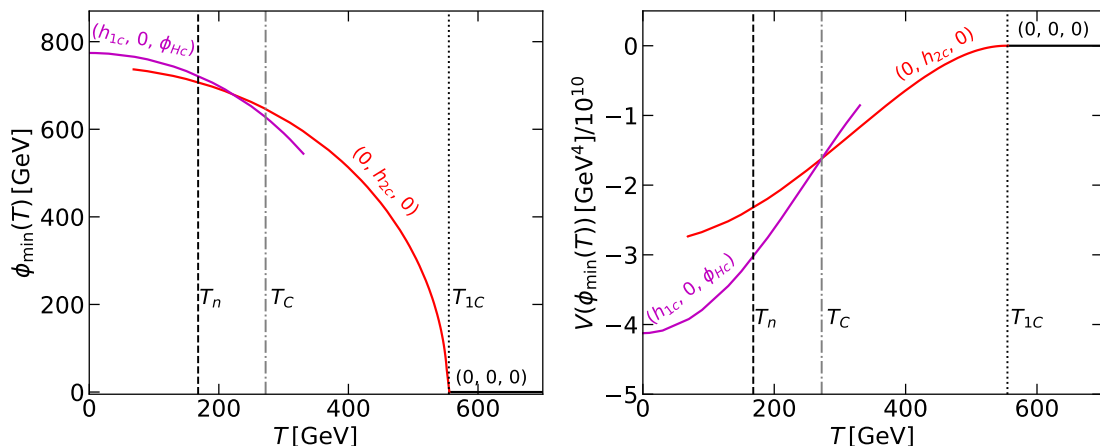


Figure 3. The evolution of $\phi_{\min}(T) = \sqrt{h_{1c}^2(T) + h_{2c}^2(T) + \phi_{Hc}^2(T)}$ (left panel) and the minimal of the effective potential (right panel) as functions of temperature. The solid black, red and purple lines represent the $(0, 0, 0)$, $(0, h_{2c}, 0)$ and $(h_{1c}, 0, \phi_{Hc})$ phases. The dotted, dash-dotted and dashed lines indicate the critical temperatures T_{1C} , T_C and nucleation temperature T_n respectively. Here we fix the model parameter space as $m_{h_2} = 745$ GeV, $m_{H^\pm} = 374$ GeV, $m_D = 320$ GeV, $m_{W'} = 0.115$ GeV, $\theta_1 = 0.235$ rad, $\theta_2 = 0.32$ rad, $m_{fH} = 1$ TeV, $g_X = 1.17 \times 10^{-4}$ and $m_X = 0.25$ GeV.

the quantity

$$\phi_{\min}(T) = \sqrt{h_{1c}^2(T) + h_{2c}^2(T) + \phi_{Hc}^2(T)} \quad (38)$$

to trace the evolution of the vacuum and fix the model parameter space as $m_{h_2} = 745$ GeV, $m_{H^\pm} = 374$ GeV, $m_D = 320$ GeV, $m_{W'} = 0.115$ GeV, $\theta_1 = 0.235$ rad, $\theta_2 = 0.32$ rad, $m_{fH} = 1$ TeV, $g_X = 1.17 \times 10^{-4}$ and $m_X = 0.25$ GeV. One can see that $m_X \sim 2m_{W'}$ so that the DM relic density satisfies the Planck observation through the resonant annihilation [146, 147, 152]. Hereafter, we label this benchmark point as **BM**. We use `PhaseTracer` package [206] to find the phases and calculate the critical temperatures. At high-T, the stable vacuum is in a symmetric phase $(0, 0, 0)$. As the temperature decreases, a continuous transition from the symmetric phase to $(0, h_{2c}, 0)$ phase occurs at $T_{1C} = \sqrt{\mu_H^2 / \tilde{\Pi}_{H_2}}$, where

from (B2)

$$\tilde{\Pi}_{H_2} = \frac{1}{12} (10\lambda_H - \lambda'_H + 2\lambda_{H\Phi} + \lambda'_{H\Phi}) + \frac{1}{16} (3g^2 + g'^2 + 3g_H^2 + g_X^2) , \quad (39)$$

and $\mu_H^2 = \lambda_H v^2 + \lambda_{H\Phi} v_\Phi^2/2$ determined by the tadpole condition at tree level. At this benchmark point, $T_{1C} \sim 556$ GeV, as indicated by the dotted line. Subsequently, a new minimum $(h_{1c}, 0, \phi_{Hc})$ appears at $T = T_C \simeq 272$ GeV², as indicated by the dash-dotted line. These two phases, $(0, h_{2c}, 0)$ and $(h_{1c}, 0, \phi_{Hc})$, are degenerate and separated by a barrier, which is a characteristic feature of a FOEWPT. As the temperature drops below T_C , the system undergoes a phase transition through the formation of bubbles, with the stable vacuum inside the bubbles being $(h_{1c}, 0, \phi_{Hc})$, and the metastable vacuum outside being $(0, h_{2c}, 0)$. The black dashed line in Fig. 3 represents the nucleation temperature, $T_n \simeq 168$ GeV, at which the formation rate of bubbles is about one per Hubble volume.

The h -parity which was broken at the metastable vacuum at high-T has been restored at the stable electroweak vacuum at lower temperature. Thus one has realized symmetry anti-restoration of a discrete symmetry in the model. While the occurrence of symmetry restoration at high-T is quite common in spontaneously broken global and gauge theories, the possible occurrence of symmetry anti-restoration at lower temperature was first pointed out by Weinberg [106] (See also [109, 207–210]). It has been used to solve the $U(1)$ magnetic monopole problem in grand unified models [211, 212]. Here we have an instance of a discrete symmetry.

C. Numerical result for two-step phase transition

We investigate the parameter space of the model that gives rise to the two-step phase transition pattern, as depicted in the right panel of Fig. 1 where $s \equiv \phi_{Hc}$,

² See Appendix E for the analytical expression of T_C .

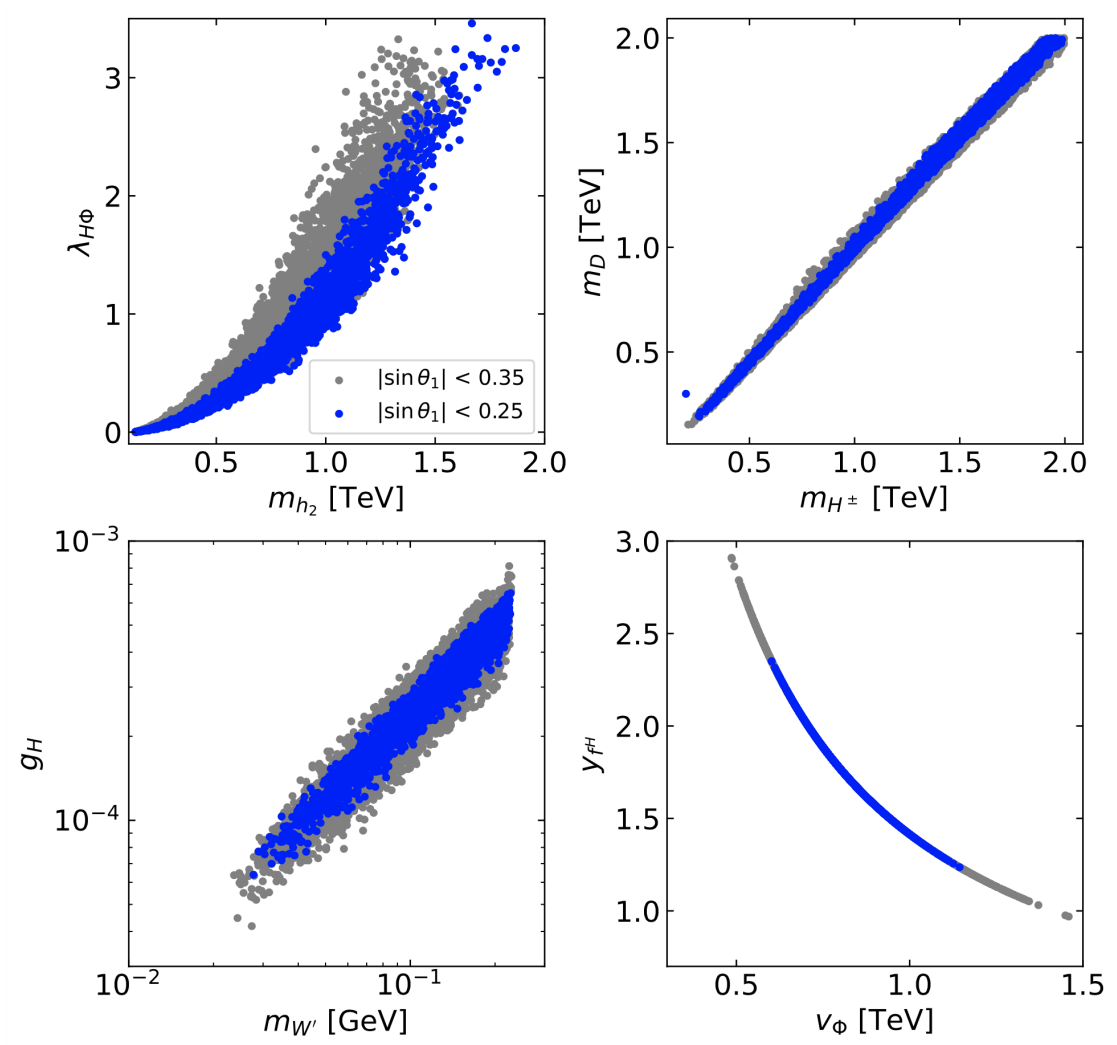


Figure 4. Viable model parameter regions for the two-step phase transition with different constraints on the mixing angles θ_1 . The gray and blue regions indicate $|\sin \theta_1| < 0.35$ and $|\sin \theta_1| < 0.25$, respectively.

$h_1 \equiv h_{1c}$ and $h_2 \equiv h_{2c}$. We first explore the parameter region that satisfies all the theoretical and experimental constraints discussed in the previous section. Next, we utilize the `PhaseTracer` package [206] to trace the minima of the effective potential as the temperature varies and to calculate the critical temperatures. To sample the parameter space in the model, we employ MCMC scans using `emcee` [213]. The

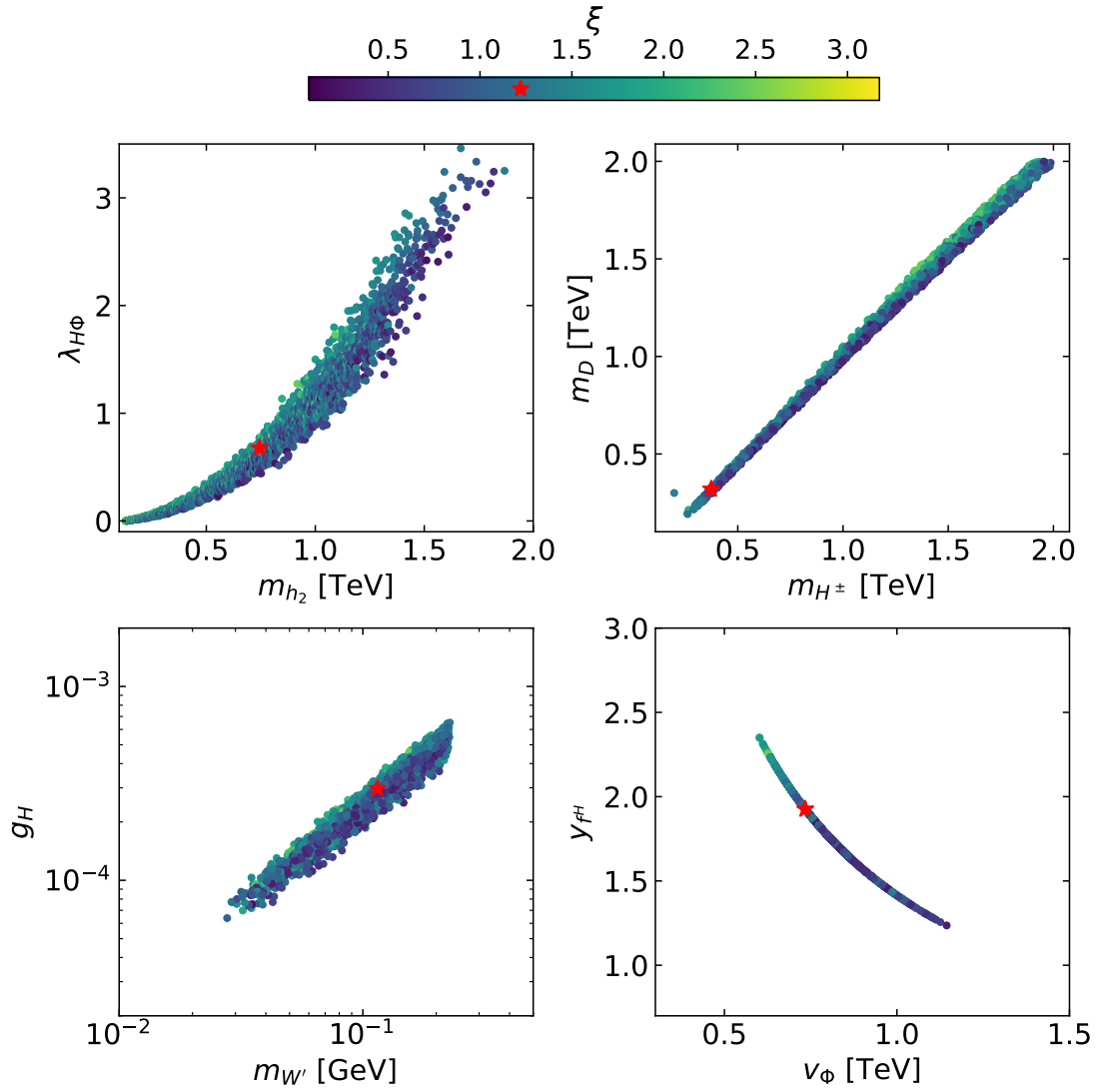


Figure 5. Viable model parameter region for the two-step phase transition, correlated with the phase transition strength. The color legend on the top indicates the value of $\xi = v_C/T_C$ where $v_C = h_{1c}(T_C)$ for the second transition. The red star represents the benchmark point **BM**.

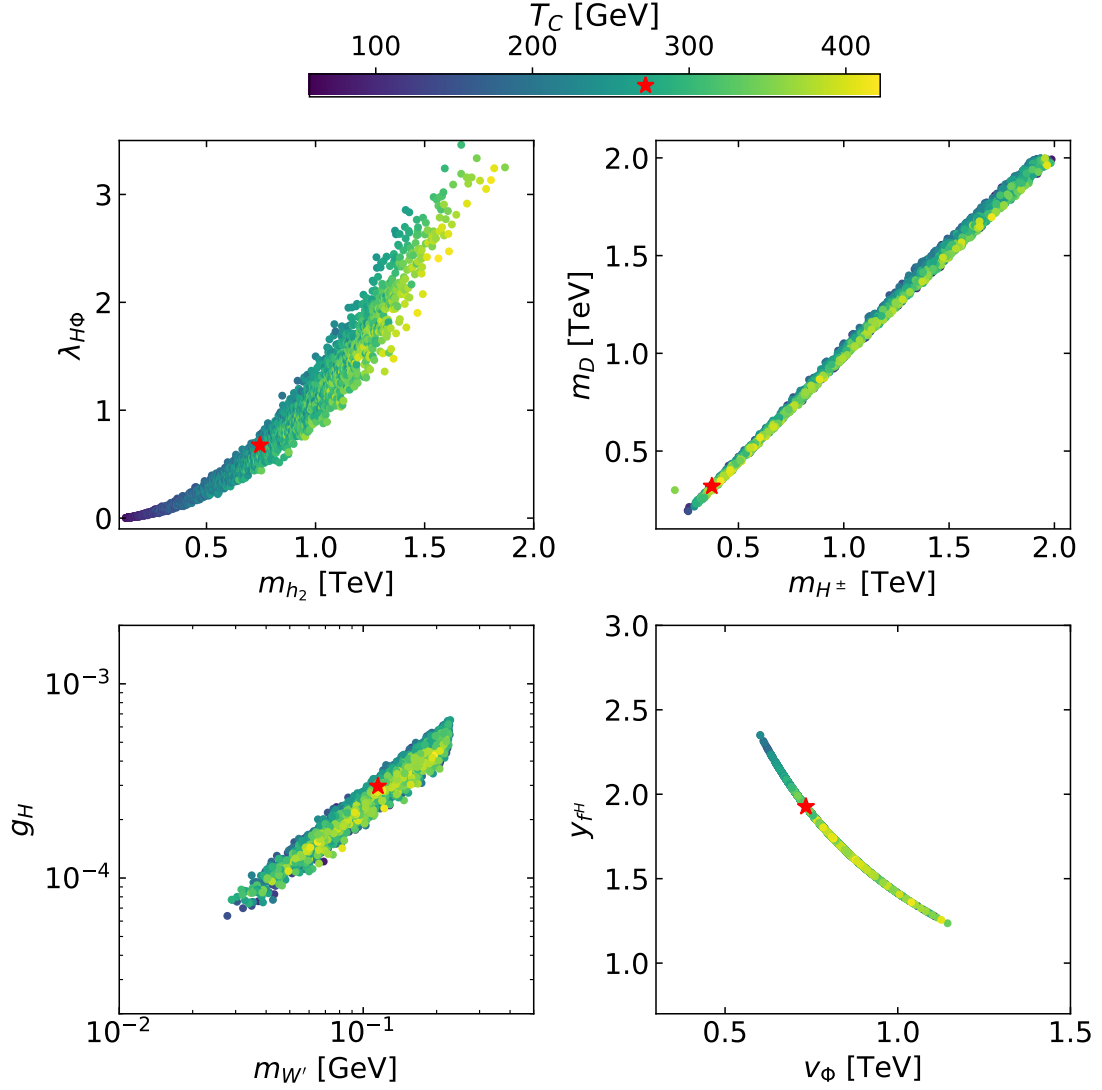


Figure 6. Viable model parameter region for the two-step phase transition, correlated with the critical temperature for the second transition. The color legend on the top indicates the critical temperature T_C for the second transition. The red star represents the benchmark point **BM**.

scanning ranges of model parameters are set as follows,

$$m_{h_2}/\text{GeV} \in (130, 2000), \quad (40)$$

$$m_{H^\pm}/\text{GeV} \in (80, 2000), \quad (41)$$

$$m_D/\text{GeV} \in (10, 2000), \quad (42)$$

$$m_{W'}/\text{GeV} \in (0.01, 50), \quad (43)$$

$$\theta_{1,2}/\text{rad} \in \left(-\frac{\pi}{2}, \frac{\pi}{2}\right), \quad (44)$$

$$g_X \in (10^{-6}, 10^{-2}), \quad (45)$$

$$M_X/\text{GeV} \in (10^{-3}, 10^2), \quad (46)$$

and we fix $m_{fH} = 1$ TeV.

Given the viable model parameter space, we find that the FOPT is most likely to occur in the second step of a two-step phase transition, as sketched in the right panel of Fig. 1 where $s \equiv \phi_{Hc}$, $h_1 \equiv h_{1c}$ and $h_2 \equiv h_{2c}$. The parameter space conducive to this two-step phase transition is depicted in Fig. 4 with different choices of the constraint on the mixing angle θ_1 . The gray area denotes $|\sin \theta_1| < 0.35$, a constraint derived from Higgs signal strength data measured at the CMS experiment, while the blue area indicates $|\sin \theta_1| < 0.25$, a requirement based on the combined Higgs signal strength data from both the ATLAS and CMS experiments. We observe that imposing a stringent constraint on θ_1 leads to a significant reduction in the viable parameter space necessary to achieve the two-step phase transition. Specifically, upon comparing the gray and blue regions in Fig. 4, a tighter constraint on $|\sin \theta_1|$ requires a smaller value for $\lambda_{H\Phi}$ and a narrower region on the (m_{H^\pm}, m_D) and $(m_{W'}, g_H)$ planes. Additionally, it results in stronger upper and lower bounds on v_ϕ .

In Fig. 5, we showcase results for $|\sin \theta_1| < 0.25$. The color within this figure indicates the strength of the EWPT in the second step, denoted here by $\xi = v_C/T_C$ ³, where $v_C = h_{1c}(T_C)$, which remains gauge invariant under the high-T

³ Not to be confused with the gauge fixing parameter having the same symbol discussed in

treatment of the effective scalar potential. If one takes a glimpse back at the left panel of Fig. 3, v_C is the intersection point between the purple and dash-dotted lines. A commonly accepted criterion to avoid the washout of baryon number generated during the phase transition is $\xi \geq 1$ [145]. We find that $\xi \lesssim 3.2$ in our scanning region. Similar to Fig. 5, Fig. 6 show the viable parameter region, but with the color indicating the critical temperature T_C . Interestingly, T_C lies within the electroweak scale.

As shown in the top-left panel of Fig. 5, for a fixed value of m_{h_2} , an increase in the quadratic coupling $\lambda_{H\Phi}$ leads to a larger ξ and therefore a stronger phase transition. This occurs due to the presence of a tree-level barrier, the height of which is proportional to $\lambda_{H\Phi}$, in the second step of the phase transition. This effect has been extensively studied in SM extensions involving gauge singlets [6, 8, 11, 20] and real triplets [108, 110, 198]. Additionally, an increase in $\lambda_{H\Phi}$ also results in a lower critical temperature, as shown in the top-left panel of Fig. 6.

In the top-right panel of Fig. 5 or 6, the viable parameter space projected on the (m_{H^\pm}, m_D) plane shows a distinct shape, which is due to the recent precision measurement of the W boson mass by the CDF-II collaboration [152]⁴. Furthermore, this panel indicates that the dark Higgs and charged Higgs must satisfy lower bounds of $m_{H^\pm} \gtrsim 200$ GeV and $m_D \gtrsim 150$ GeV, respectively.

We observe that in this model, even for scalar masses on the order of 1 TeV, the two-step phase transition can occur, which contrasts with the generic upper bound of ~ 700 GeV as discussed in Ref. [122]. This larger range for the new scalar masses arises because the extra scalar boson considered in Ref. [122] obtains its mass solely from the SM doublet VEV v , whereas the inert Higgs doublet H_2 in G2HDM is also a member of a doublet under a hidden $SU(2)_H$ that is broken by a new VEV v_Φ , thereby generating additional contributions to their masses. For

Appendix D.

⁴ If one instead uses the data from the PDG [214], excluding the CDF-II measurement, the most significant change in the parameter space is the mass splitting between the charged Higgs and the dark Higgs. The PDG data favor a smaller mass splitting [152].

example, two-step transition requires $T_{1C} > T_C$ and thus

$$\mu_H^2 = \Pi_{H_2}(T_{1C}) > \Pi_{H_2}(T_C) \sim \Pi_{H_2}(T_{EW}), \quad (47)$$

where T_{1C} (T_C) is the critical temperature for the first (second) step and T_{EW} is the electroweak temperature. Assuming a small mixing between h -parity odd scalar fields, one can obtain the dark Higgs boson mass at zero temperature as

$$m_D \simeq m_{H_2^0} = \sqrt{-\mu_H^2 + \lambda_H v^2 + \frac{1}{2}(\lambda_{H\Phi} + \lambda'_{H\Phi})v_\Phi^2} \quad (48)$$

$$< \sqrt{-\Pi_{H_2}(T_{EW}) + \lambda_H v^2 + \frac{1}{2}(\lambda_{H\Phi} + \lambda'_{H\Phi})v_\Phi^2}. \quad (49)$$

Taking numerical values of $\lambda_H = 0.8$, $\lambda_\Phi = 1.7$, $\lambda_{H\Phi} = 2.1$, $\lambda'_{H\Phi} = 2.9$, $\lambda'_H = -3.3$ and $g_{H,X} \ll 1$, we obtain

$$m_D \simeq m_{H_2^0} \lesssim \sqrt{-1.6 T_{EW}^2 + 0.8 v^2 + 2.5 v_\Phi^2}. \quad (50)$$

With $T_{EW} = 200$ GeV and $v_\Phi = 1.3$ TeV, one can get an upper bound of $m_D \lesssim 2$ TeV.

The mass of the DM particle, $m_{W'}$, falls in the sub-GeV range of 0.02 GeV to 0.25 GeV, as revealed in the bottom-left panel of Fig. 5 or 6. This restriction range of $m_{W'}$ is due to the limits on the new gauge coupling g_H , which arises from dark photon searches [146, 147, 152], as well as the bounds on v_Φ . As shown in the bottom-right panel of Fig. 5 or 6, v_Φ falls within the range of [0.5 TeV, 1.4 TeV]. This range represents a combination of collider constraints illustrated in Fig. 2 and the two-step phase transition condition requirement for $\lambda_{H\Phi}$, as shown in the top-left panel of Fig. 5 or 6. With the mass of the heavy hidden fermions fixed at 1 TeV, a relatively large value of the Yukawa coupling y_{fH} is required in the small region of v_Φ . Nevertheless y_{fH} is still below $\sqrt{4\pi}$ allowed by perturbative unitarity arguments. Additionally, smaller regions of v_Φ show a trend towards larger values of ξ . Finally, the bottom-right panel of Fig. 6 shows that T_C increases in regions of larger values of v_Φ .

IV. STOCHASTIC GRAVITATIONAL WAVES

During a cosmological FOEWPT, the production of GWs is a result of several distinct mechanisms. In particular, primary sources of GW generation are bubble collisions, sound waves, and magneto-hydrodynamic (MHD) turbulence [133, 215]. For bubble collisions, the GW is generated from the stress energy localized at the bubble wall. Such GW spectra have been estimated analytically [216] and numerically under the so-called thin-wall and envelope approximations respectively [217–220]. On the other hand, the motion of the fluid in the plasma during the phase transition generates sound waves. As the sound waves dissipate, they transfer energy into GWs [221–224]. The GW spectrum from this source typically relies on large scale lattice simulations [221, 224–226]. However, an analytical modeling can reproduce the spectra from simulations reasonably well based on the sound shell model [227, 228]. Turbulence can also be induced in the plasma by percolation, particularly MHD turbulence, given that the plasma is fully ionized. This also leads to the production of GWs [229–233]. The significance of each contribution to GW generation is heavily influenced by the characteristics and dynamics of the phase transition. The velocity of the bubble wall is a critical factor in this regard. If the wall velocity is slow, the thermal bath can effectively absorb the energy released during the phase transition, leading to suppression of the GW spectrum. On the other hand, if the bubble wall velocity is relativistic, a considerable amount of energy can be converted into bulk motion. In this study we consider a so-called *non-runaway bubbles* in which the bubble expansion in the plasma can result in the attainment of a relativistic terminal velocity [215]. In this case, the contributions from the sound waves and the MHD turbulence are dominant. For recent reviews on GW signals and cosmological first order phase transitions, we refer our readers to [234, 235].

In order to calculate the GW signals resulting from the FOEWPT, the following 4 parameters must be determined: the nucleation temperature, T_n ; the fraction

of energy released from the phase transition to the total radiation energy density at the nucleation temperature, α ; the inverse duration of the phase transition β (usually normalized by H_* , the Hubble rate at the percolation temperature); and the velocity of the bubble wall, v_w . The wall velocity can be calculated from micro-dynamics of particle interactions with the Higgs condensate, its precise value remains undetermined due to the theoretical uncertainties in the calculations. Here we choose $v_w = 0.95$ in our analysis. The sensitivity of GW detectors can significantly depend on values of bubble wall velocity [115]. Within the viable parameter space in G2HDM, we find that sensitivity of LISA detector is maximized around $v_w \simeq [0.7, 0.8]$. Higher values of v_w slightly reduce sensitivity, while it drops dramatically for smaller v_w ($v_w < 0.6$).

The nucleation temperature is usually determined by solving the following equation

$$\int_{T_n}^{\infty} \frac{dT}{T} \frac{\Gamma(T)}{H(T)^4} \simeq 1, \quad (51)$$

where $\Gamma(T)$ is the tunneling probability per unit time per unit volume, which is calculated using the following formula

$$\Gamma(T) \simeq T^4 \left(\frac{\mathcal{S}_3}{2\pi T} \right)^{3/2} e^{-\mathcal{S}_3/T}. \quad (52)$$

Here \mathcal{S}_3 represents the three-dimensional Euclidean action corresponding to the critical bubble, which is given by

$$\mathcal{S}_3 = \int_0^{\infty} dr r^2 \left[\frac{1}{2} \left(\frac{d\hat{\phi}(r)}{dr} \right)^2 + V(\hat{\phi}, T) \right], \quad (53)$$

where $\hat{\phi}$ denotes a collection of classical scalar fields ⁵ that minimizes the action \mathcal{S}_3 and are determined by solving the following equation of motion

$$\frac{d^2 \hat{\phi}}{dr^2} + \frac{2}{r} \frac{d\hat{\phi}}{dr} = \frac{dV(\hat{\phi}, T)}{d\hat{\phi}}, \quad (54)$$

⁵ In the present context, $\hat{\phi} = \{h_{1c}(r, T), h_{2c}(r, T), \phi_{Hc}(r, T)\}$.

with the boundary conditions

$$\lim_{r \rightarrow \infty} \hat{\phi}(r) = 0, \quad \left. \frac{d\hat{\phi}}{dr} \right|_{r=0} = 0. \quad (55)$$

Here we utilize the `CosmoTransitions` package [236] to numerically solve the bounce equation in Eq. (54) and subsequently calculate the action. A rough estimation of the nucleation temperature, T_n , can be obtained by solving the following nucleation condition

$$\mathcal{S}_3(T_n)/T_n \simeq 140. \quad (56)$$

The inverse duration parameter β can be calculated using the following equation

$$\frac{\beta}{H_*} = T_* \left. \frac{d(\mathcal{S}_3/T)}{dT} \right|_{T_*}, \quad (57)$$

where T_* is the temperature at which GWs are generated and it is expected that $T_* \simeq T_n$, and H_* is the Hubble rate at T_* . The parameter α can be obtained by

$$\alpha = \frac{\rho_{\text{vac}}}{\rho_{\text{rad}}^*} = \frac{1}{\rho_{\text{rad}}^*} \left[T \frac{\partial \Delta V(T)}{\partial T} - \Delta V(T) \right] \Big|_{T_*}, \quad (58)$$

where ρ_{vac} is the vacuum energy density, $\rho_{\text{rad}}^* = g_* \pi^2 T^4 / 30$ is the total radiation energy density with $g_* = 106.75$ being the number of relativistic degrees of freedom at T_* , and ΔV is the difference in scalar potential between the lower and higher phases.

With these portal parameters, we utilize the `PTPlot` package [225, 237] to calculate the GW spectrum. To quantify the detectability of the signals, one can define the signal-to-noise ratio (SNR) [237]

$$\text{SNR} = \sqrt{\mathcal{T} \int_{f_{\text{min}}}^{f_{\text{max}}} df \left[\frac{h^2 \Omega_{\text{GW}}(f)}{h^2 \Omega_{\text{exp}}(f)} \right]^2}, \quad (59)$$

where \mathcal{T} is the duration of the observation period in years, $h^2 \Omega_{\text{GW}}(f)$ represents the GW energy fraction spectrum from the FOEWPT and $h^2 \Omega_{\text{exp}}(f)$ is the sensitivity of the experimental setup. It is commonly accepted that a SNR value of 10 is

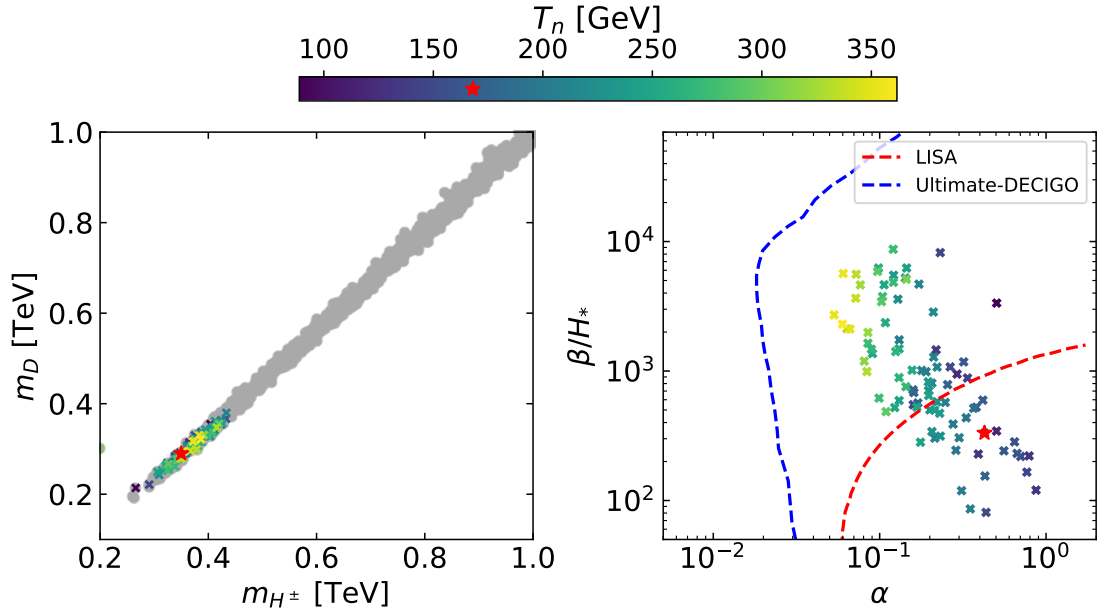


Figure 7. Strong FOEWPT points in the two-step phase transition projected on the (m_{H^\pm}, m_D) plane (left) and the $(\alpha, \beta/H_*)$ plane (right). The light gray points on the left panel indicate the points fulfilling the two-step phase transition, while the colored cross points in both panels indicate the surviving points after applying the nucleation condition. The color legend on the top indicates the nucleation temperature T_n . The dashed red and blue lines represent the LISA with a SNR = 10 and Ultimate-DECIGO sensitivity respectively. The red star represents the benchmark point **BM**.

the threshold for detection. For the benchmark point **BM** depicted in Fig. 3, the values of T_n , α , β/H_n and LISA SNR we obtained are 168 GeV, 0.43, 332 and 144 respectively.

By applying the nucleation condition described in Eq. (56) to the two-step phase transition data points, we find that only approximately 3% of the data points meet this criterion. While the range of other parameters remains largely unchanged after applying the nucleation condition, the upper bound on the masses of the charged Higgs and dark Higgs is significantly altered. In particular, as shown

in the left panel of Fig. 7, it is required that $m_{H^\pm} \lesssim 450$ GeV and $m_D \lesssim 400$ GeV. Additionally, as shown in the same panel, we can see that the value of the nucleation temperature T_n tends to increase in the regions of larger masses of the charged Higgs and dark Higgs.

The right panel of Fig. 7 shows the surviving points on the $(\alpha, \beta/H_*)$ plane after applying the nucleation condition. As a result, the range of β/H_* is approximately $(50, 10^4)$ and the range of α is approximately $(0.05, 1)$. All prediction points lie within the sensitivity range of the Ultimate-DECIGO detector (dashed blue line) [142] and a part of them lies within the LISA sensitivity region with a SNR > 10 [237]⁶. A larger value of α suggests more energy from the plasma being converted into GWs, while a smaller value of β/H_* implies a longer duration of the strong first-order phase transition, thus leading to an enhancement of the GW energy spectrum.

The predicted energy spectrum peaks of GWs as a function of frequency are presented in Fig. 8. As a result, the generated GWs resulting from the FOEWPT in the two-step transition have peak frequencies within the range of $(\sim 10^{-4}, \sim 0.2)$ Hz and peak yields vary in the range $(\sim 10^{-17}, \sim 10^{-9})$. These peak yields are expected to be accessible at BBO, LISA, (Ultimate-)DECIGO, TianQin and Taiji detectors in the future. For demonstration purposes, we show the GW spectrum generated from the benchmark point **BM** as the solid red line in Fig. 8. The benchmark point is selected with a relatively high value of α in order to increase the magnitude of the generated GWs, making it possible to be accessible by BBO, LISA, and (Ultimate-)DECIGO.

⁶ Here, in order to obtain the Ultimate-DECIGO and LISA sensitivity lines, we take $T_n = 100$ GeV and $v_w = 0.95$ for the purpose of illustration.

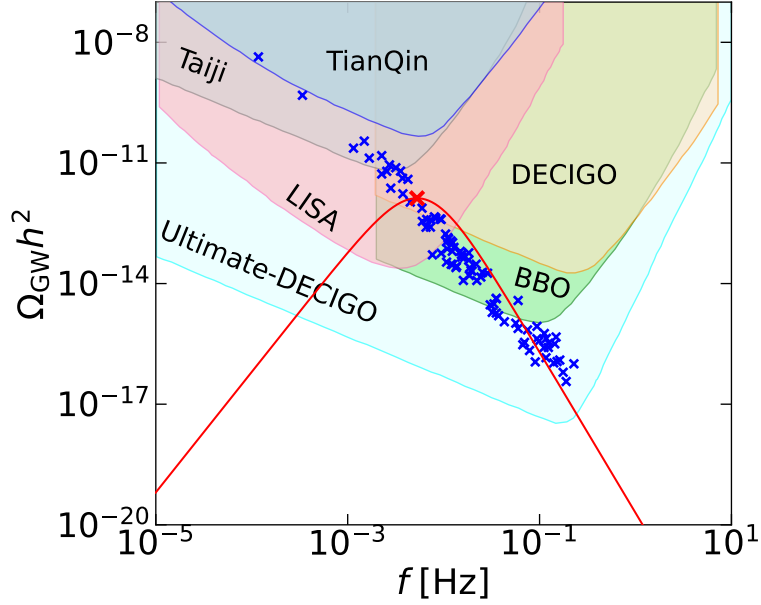


Figure 8. The GW energy spectrum generated from the benchmark point **BM** is represented by the solid red line with its peak indicated by the red cross. Peaks of the GW energy spectrum from other surviving points generated from a two-step phase transition are indicated by blue cross points. The experimental sensitivities of various GW detectors, including Taiji, TianQin, DECIGO, Ultimate-DECIGO, BBO, and LISA, are indicated by shaded color regions.

V. DARK MATTER DIRECT DETECTION PROSPECTS

In recent decades, significant advancements have been made in the design and construction of direct-detection experiments aimed at detecting weakly interacting massive particles (WIMPs) that are potential candidates for DM. Notable examples of these experiments include CRESST III [170], DarkSide-50 [171, 172], XENON1T [173, 174], PandaX-4T [176], and LZ [177]. These experiments have led to significant improvements in searches for few keV-scale nuclear recoils, which are indicative of spin-independent scattering of WIMPs with masses greater than

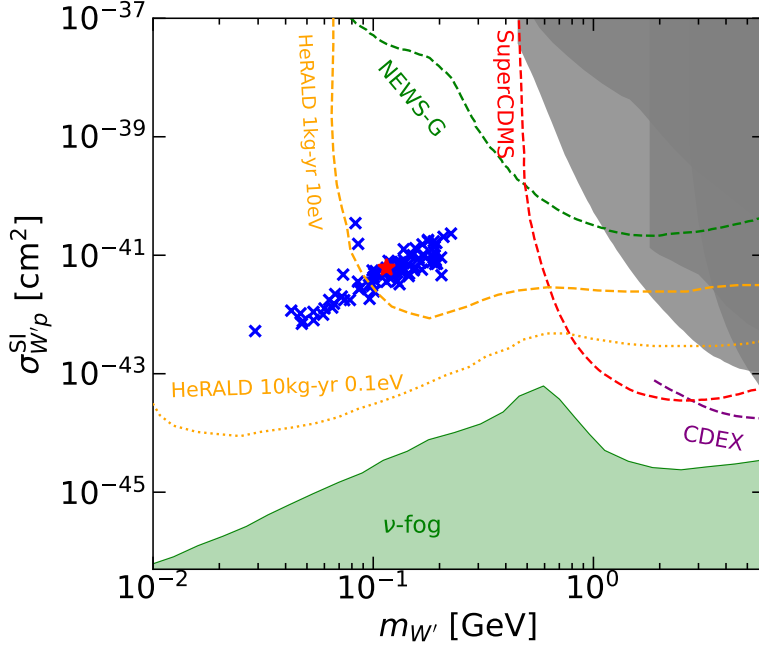


Figure 9. The spin-independent DM-proton scattering cross section as a function of DM mass for the parameter space probed by the GW signals at the Ultimate-DECIGO detector. The gray regions represent the exclusion limits from current DM direct detection experiments. The dashed green, dashed red, dashed purple, dashed orange and dotted orange lines show the expected sensitivities of future DM direct detection experiments at NEWS-G [238], SuperCDMS [239], CDEX [240], HeRALD [241] with 1 kg-year of exposure and 10 eV of energy threshold, and with 10 kg-year of exposure and 0.1 eV of energy threshold, respectively. The green region represents the neutrino fog background. The red star indicates benchmark point **BM**.

1 GeV. While the next generation of experiments, such as PandaX30T [242], XENONnT [243], DarkSide-20k [244], and DARWIN [245], are expected to explore a large fraction of the theoretically well-motivated parameter space for this mass range and even reach the neutrino fog, there is growing interest in exploring DM with sub-GeV mass ranges [246].

However, the detection of sub-GeV DM remains challenging due to the low nuclear recoil energies involved and the finite detector thresholds. Nevertheless, new technologies capable of achieving lower detector energy thresholds, down to meV–eV scales, are being proposed [246]. For example, the HeRALD proposal [241] involves an array of microchannel plates and photomultiplier tubes that can measure ionization signals resulting from DM interactions with helium nuclei. This approach enables HeRALD to reach energy thresholds as low as a few meV, thus making it suitable for probing DM in the sub-GeV mass region.

As demonstrated before, a two-step transition for achieving a strong FOEWPT in the G2HDM leads to the prediction that the DM mass falls within the sub-GeV range. This prediction renders the DM candidate a suitable candidate for exploration in upcoming DM direct detection experiments. Fig. 9 shows the spin-independent DM-proton scattering cross-section as a function of DM mass for the parameter space being probed by gravitational wave detectors. While NEWS-G [238], SuperCDMS [239], and CDEX [240] are designed to probe DM with masses around and above 1 GeV, HeRALD with 1 kg-year of exposure and 10 eV of detector energy threshold can probe part of our parameter space that predicts gravitational wave signals. HeRALD can fully cover our parameter space with 10 kg-year of exposure and a detector energy threshold of 0.1 eV. Therefore, it highlights an interesting interplay between future DM direct detection and GW signal searches.

VI. CONCLUSIONS

We investigate the electroweak phase transition and the possibility of detecting GW signals resulting from the phase transition in the simplified G2HDM. The simplified G2HDM is a well-motivated dark matter model with a hidden non-abelian gauge boson $W'^{(p,m)}$ serving as a DM candidate. The stability of the

DM candidate is protected by an accidental h -parity in the model. We take into account both theoretical and experimental constraints, with the latter including Higgs experimental data, electroweak precision measurements, dark photon and DM direct search experiments.

We derive the effective potential in the simplified G2HDM, including the one-loop finite temperature correction with daisy resummation. The effective potential consists of three background fields $(h_{1c}, h_{2c}, \phi_{Hc})$ that give rise to rich patterns of phase transition. We require $h_{2c} = 0$ at zero temperature to anti-restore the h -parity and analyze the possible first-order electroweak phase transition in the early universe.

We identify several rather distinctive features of the simplified G2HDM as follows:

- A two-step phase transition pattern is possible, where the symmetric phase transfers to the inert doublet h_{2c} direction first and subsequently to the electroweak vacuum phase with a non-zero hidden doublet VEV v_Φ in addition to the SM doublet VEV v as the temperature decreases. Using the high-T approximation in the effective potential that manifests gauge invariance, we found that the former transition is a second-order phase transition, while the latter can be first-order due to a tree-level barrier. The first step breaks h -parity and the second step restores it.
- Unlike the conventional Z_2 symmetry model, where the two-step FOEWPT imposes strict upper bounds on new scalar masses, these bounds can be relaxed in G2HDM. In G2HDM, the new scalars receive contributions to their masses from a hidden sector VEV, allowing for somewhat larger BSM scalar masses to be compatible with a FOEWPT. However, due to the perturbative limit on the couplings and the bubble nucleation condition for GWs, scalar masses can only reach $\mathcal{O}(1 \text{ TeV})$. In particular, the extra h -parity even scalar boson mass m_{h_2} can reach 1.8 TeV, the h -parity odd scalars D and H^\pm

can only reach up to 500 GeV. Our findings also suggest that the Higgs portal coupling $\lambda_{H\Phi}$ needs to be sizable and the VEV v_Φ of the $SU(2)_L$ singlet/ $SU(2)_H$ doublet scalar Φ_H needs to be within the range of 0.5 TeV to 1.4 TeV.

- The predicted GW energy spectrum from two-step FOEWPT in this model can be probed in the next-generation GW detectors. In particular, we find that the peak frequencies lie within the range of ($\sim 10^{-4}, \sim 0.2$) Hz, and the peak yields vary from $\sim 10^{-17}$ to $\sim 10^{-9}$. These frequencies and yields can be covered by BBO, LISA, (Ultimate-)DECIGO, TianQin, and Taiji in the future.
- Interestingly, these GW probed regions can also be searched for in the future dark matter direct detection experiments, such as the superfluid-He target detectors. While it is possible for the DM candidate to be heavy [152], we have concentrated on the light mass region due to its potential accessibility by future direct detection experiments.
- Albeit the above distinctive features are obtained here in a specific model of G2HDM, it is conceivable that they might be present in other class of models, for instance in certain limit of the IHDM, augmented further by a scalar singlet. After all, the scalar potential of G2HDM can be regarded as a gauged version of the one from IHDM, supplemented by a hidden $SU(2)_H$ doublet Φ_H which is nevertheless a SM singlet.

Finally, we note that the results in this work are presented at leading order, *i.e.*, using the high-T approximation in the effective potential. Higher-order corrections that include both a systematical thermal resummation and a properly gauge-invariant treatment are needed to be taken into account to obtain more accurate predictions. This can be done by using the state-of-the-art dimensional reduction method reducing the simplified G2HDM to a 3d effective field theory. To fully

resolve the IR problem and properly identify the boundary between FOEWPT-viable and crossover regions of the parameter space, lattice studies are required. We will defer this exploration to the future.

ACKNOWLEDGMENTS

We would like to thank Eibun Senaha for useful discussions. This work was supported in part by the National Natural Science Foundation of China, grant Nos. 19Z103010239, 12350410369 (VQT) and 11975150, 12375094 (MJRM) and the NSTC of Taiwan, grant Nos. 111-2112-M-001-035, 113-2112-M-001-001 (TCY) and 112-2811-M-001-089 (VQT). VQT would like to thank the Medium and High Energy Physics Group at the Institute of Physics, Academia Sinica, Taiwan for their hospitality during the course of this work.

Appendix A: Field Dependent Masses

We will work in the Landau gauge where all the Goldstone bosons are massless and the ghost contributions can be ignored. The thermal mass corrections for the scalar fields ($\Pi_{H_1}(T)$, $\Pi_{H_2}(T)$ and $\Pi_{\Phi_H}(T)$) and the longitudinal components of the gauge fields ($\Pi_W(T)$, $\Pi_B(T)$, $\Pi_{W'}(T)$ and $\Pi_X(T)$) are also included in this work for the daisy resummation. These thermal mass corrections are given in Appendix B.

1. Gauge Bosons

In what follows, we will suppress the temperature dependence of the constant background fields $h_{ic}(T)$ and $\phi_{Hc}(T)$ and denote them simply as h_{ic} and ϕ_{Hc} unless stated otherwise. For convenience, we define the following combinations of the background fields

$$h_{\pm}^2 \equiv h_{1c}^2 \pm h_{2c}^2, \quad (\text{A1})$$

$$h_{\pm\Phi}^2 \equiv h_{\pm}^2 \pm \phi_{Hc}^2. \quad (\text{A2})$$

There is only one electric charged vector boson, the SM W^{\pm} , with field depen-

dent mass given by

$$m_{W_T^\pm}^2 = \frac{1}{4}g^2h_+^2, \quad (\text{A3})$$

$$\bar{m}_{W_L^\pm}^2 = m_{W_T^\pm}^2 + \Pi_W(T). \quad (\text{A4})$$

In general, W'^2 doesn't mix with other gauge fields and its field dependent mass is given by

$$m_{W_T'^2}^2 = \frac{1}{4}g_H^2h_{+\Phi}^2, \quad (\text{A5})$$

$$\bar{m}_{W_L'^2}^2 = m_{W_T'^2}^2 + \Pi_{W'}(T). \quad (\text{A6})$$

All the other 5 gauge bosons associated with the remaining 5 generators in G2HDM are electrically neutral and in general mixed together. In the basis of $\{B, W^3, X, W'^3, W'^1\}$, one finds the transverse mass matrix

$$M_{N_T}^2 = \begin{pmatrix} \frac{1}{4}g'^2h_+^2 & -\frac{1}{4}g'gh_+^2 & \frac{1}{4}g'g_Xh_+^2 & +\frac{1}{4}g'g_Hh_-^2 & \frac{1}{2}g'g_Hh_{1c}h_{2c} \\ -\frac{1}{4}gg'h_+^2 & \frac{1}{4}g^2h_+^2 & -\frac{1}{4}gg_Xh_+^2 & -\frac{1}{4}gg_Hh_-^2 & -\frac{1}{2}gg_Hh_{1c}h_{2c} \\ \frac{1}{4}g_Xg'h_+^2 & -\frac{1}{4}g_Xgh_+^2 & \frac{1}{4}g_X^2h_{+\Phi}^2 + m_X^2 & \frac{1}{4}g_Xg_Hh_{-\Phi}^2 & \frac{1}{2}g_Xg_Hh_{1c}h_{2c} \\ \frac{1}{4}g_Hg'h_-^2 & -\frac{1}{4}g_Hgh_-^2 & \frac{1}{4}g_Hg_Xh_{-\Phi}^2 & \frac{1}{4}g_H^2h_{+\Phi}^2 & 0 \\ \frac{1}{2}g_Hg'h_{1c}h_{2c} & -\frac{1}{2}g_Hgh_{1c}h_{2c} & \frac{1}{2}g_Hg_Xh_{1c}h_{2c} & 0 & \frac{1}{4}g_H^2h_{+\Phi}^2 \end{pmatrix}. \quad (\text{A7})$$

It is clear that for $h_{1c}h_{2c} \neq 0$, W'^1 can mix with B , W^3 and X . Thus in general W'^1 and W'^2 have different masses and do not combine into two complex conjugate fields (denoted by $W'^{(p,m)} = (W'^1 \mp iW'^2)/\sqrt{2}$ in previous studies) unless one of the h_{1c} and h_{2c} or both vanishes! Note that we have included a Stueckelberg mass m_X for the $U(1)_X$ while for the $U(1)_Y$ we set its Stueckelberg mass M_Y to be zero due to phenomenological reasons discussed in earlier works. We also do not include kinetic mixing among the two $U(1)$ s.

Despite its unappealing look, the determinant of Eq. (A7) vanishes for arbitrary values of h_{1c} , h_{2c} and ϕ_{Hc} , all of which can be different from their vacuum values of

v_1 , v_2 and v_Φ respectively at zero temperature. So it has at least one zero eigenvalue which can be identified as the photon ⁷. The exact results of the eigenvalues of $\mathcal{M}_{N_T}^2$ depend on the detailed symmetry breaking patterns. We will denote the eigenstates of Eq. (A7) as the transverse γ_T and Z_{iT} with eigenvalues $m_{\gamma_T}^2 = 0$ and $m_{Z_{iT}}^2$ for $i = 1, 2, 3$, and 4 respectively.

For the longitudinal components of the neutral gauge bosons, we have to include their thermal masses as well. The mass matrix now becomes

$$\overline{M}_{N_L}^2 = M_{N_T}^2 + \begin{pmatrix} \Pi_B(T) & 0 & 0 & 0 & 0 \\ 0 & \Pi_W(T) & 0 & 0 & 0 \\ 0 & 0 & \Pi_X(T) & 0 & 0 \\ 0 & 0 & 0 & \Pi_{W'}(T) & 0 \\ 0 & 0 & 0 & 0 & \Pi_{W'}(T) \end{pmatrix}. \quad (\text{A8})$$

We will denote the eigenstates of $\overline{M}_{N_L}^2$ in (A8) as the longitudinal γ_L and Z_{iL} with eigenvalues $\overline{m}_{\gamma_L}^2$ and $\overline{m}_{Z_{iL}}^2$ for $i = 1, 2, 3$, and 4 respectively.

Setting all the thermal masses to be zeros, $h_{1c} \rightarrow v$, $h_{2c} \rightarrow 0$ and $\phi_{Hc} \rightarrow v_\Phi$ in the above formulae, one can reproduce the tree level mass spectrum and mixings for the neutral gauge bosons presented in Sec. IIB for the zero temperature case. For instance, W'_1 and W'_2 will have the same mass and can combine into two complex fields $W'^{(p,m)} = (W'_1 \mp iW'_2)/\sqrt{2}$ which will be considered as sub-GeV DM candidate in this work.

⁷ Including a Stueckelberg mass M_Y for the hypercharge $U(1)_Y$ gauge field B would break this statement.

2. Scalar Bosons

In G2HDM, the charged scalar h_1^+ and h_2^+ in (3) mix according to the following mass matrix

$$M_C^2 = \begin{pmatrix} -\mu_H^2 + \lambda_H h_+^2 - \frac{1}{2} (\lambda'_H h_{2c}^2 - \lambda_{H\Phi} \phi_{Hc}^2) & \frac{1}{2} \lambda'_H h_{1c} h_{2c} \\ \frac{1}{2} \lambda'_H h_{1c} h_{2c} & -\mu_H^2 + \lambda_H h_+^2 - \frac{1}{2} (\lambda'_H h_{1c}^2 - \tilde{\lambda}_{H\Phi} \phi_{Hc}^2) \end{pmatrix} \quad (\text{A9})$$

Here we have defined $\tilde{\lambda}_{H\Phi} \equiv \lambda_{H\Phi} + \lambda'_{H\Phi}$. Note that M_C^2 depends on the values of μ_H^2 , its eigenvalues also depend on the detail of the symmetry breaking patterns. Including the thermal mass corrections, we have

$$\overline{M}_C^2 = M_C^2 + \begin{pmatrix} \Pi_{H_1}(T) & 0 \\ 0 & \Pi_{H_2}(T) \end{pmatrix}. \quad (\text{A10})$$

We will denote the two eigenstates as G^\pm and H^\pm and their corresponding eigenvalues of M_C^2 (\overline{M}_C^2) are $m_{G^\pm}^2$ and $m_{H^\pm}^2$ ($\overline{m}_{G^\pm}^2$ and $\overline{m}_{H^\pm}^2$) respectively. Explicitly, we have

$$\begin{aligned} \overline{m}_{G^\pm, H^\pm}^2 &= \frac{1}{4} \left\{ -2(2\mu_H^2 - \Pi_{H_+}) + (4\lambda_H - \lambda'_H) h_+^2 + (\lambda_{H\Phi} + \tilde{\lambda}_{H\Phi}) \phi_{Hc}^2 \right. \\ &\quad \left. \mp \left[\lambda_H'^2 h_+^4 - 2\lambda'_H h_-^2 (\lambda'_{H\Phi} \phi_{Hc}^2 - 2\Pi_{H_-}) + (\lambda'_{H\Phi} \phi_{Hc}^2 - 2\Pi_{H_-})^2 \right]^{1/2} \right\}, \end{aligned} \quad (\text{A11})$$

with $\Pi_{H_\pm} = (\Pi_{H_1} \pm \Pi_{H_2})$ and m_{G^\pm, H^\pm}^2 is given by (A11) with Π_{H_\pm} set to 0.

In the general spontaneous symmetry breaking in G2HDM, all the other scalar fields in the three doublets mix together according to their CP properties. This is expected since the parameters in the scalar potential of G2HDM are all real and the scalar potential is CP conserving. The real and imaginary fields have opposite CP properties and they should not mix!

For the CP-even scalars in the basis of $\{h_{\text{SM}}, h_2^0, \phi_H, G_H^1\}$, the mass matrix is

given by

$$M_S^2 = \begin{pmatrix} (\#)_{11} & 2\lambda_H h_{1c} h_{2c} & \lambda_{H\Phi} h_{1c} \phi_{Hc} & \frac{1}{2} \lambda'_{H\Phi} h_{2c} \phi_{Hc} \\ 2\lambda_H h_{1c} h_{2c} & (\#)_{22} & \tilde{\lambda}_{H\Phi} h_{2c} \phi_{Hc} & \frac{1}{2} \lambda'_{H\Phi} h_{1c} \phi_{Hc} \\ \lambda_{H\Phi} h_{1c} \phi_{Hc} & \tilde{\lambda}_{H\Phi} h_{2c} \phi_{Hc} & (\#)_{33} & \frac{1}{2} \lambda'_{H\Phi} h_{1c} h_{2c} \\ \frac{1}{2} \lambda'_{H\Phi} h_{2c} \phi_{Hc} & \frac{1}{2} \lambda'_{H\Phi} h_{1c} \phi_{Hc} & \frac{1}{2} \lambda'_{H\Phi} h_{1c} h_{2c} & (\#)_{44} \end{pmatrix}, \quad (\text{A12})$$

with the diagonal elements defined as follows

$$(\#)_{11} = -\mu_H^2 + \lambda_H(3h_{1c}^2 + h_{2c}^2) + \frac{1}{2} \lambda_{H\Phi} \phi_{Hc}^2, \quad (\text{A13})$$

$$(\#)_{22} = -\mu_H^2 + \lambda_H(h_{1c}^2 + 3h_{2c}^2) + \frac{1}{2} \tilde{\lambda}_{H\Phi} \phi_{Hc}^2, \quad (\text{A14})$$

$$(\#)_{33} = -\mu_\Phi^2 + 3\lambda_\Phi \phi_{Hc}^2 + \frac{1}{2} (\lambda_{H\Phi} h_+^2 + \lambda'_{H\Phi} h_{2c}^2), \quad (\text{A15})$$

$$(\#)_{44} = -\mu_\Phi^2 + \lambda_\Phi \phi_{Hc}^2 + \frac{1}{2} (\lambda_{H\Phi} h_+^2 + \lambda'_{H\Phi} h_{1c}^2). \quad (\text{A16})$$

Including the thermal masses, we have

$$\bar{M}_S^2 = M_S^2 + \begin{pmatrix} \Pi_{H_1}(T) & 0 & 0 & 0 \\ 0 & \Pi_{H_2}(T) & 0 & 0 \\ 0 & 0 & \Pi_{\Phi_H}(T) & 0 \\ 0 & 0 & 0 & \Pi_{\Phi_H}(T) \end{pmatrix}. \quad (\text{A17})$$

We denote the eigenvalues of M_S^2 and \bar{M}_S^2 as $m_{S_i}^2$ and $\bar{m}_{S_i}^2$ respectively for the CP-even states S_i with $i = 1, 2, 3$, and 4.

For the CP-odd scalars in the basis $\{G_1^0, G_2^0, G_H^0, G_H^2\}$, the mass matrix is

$$M_P^2 = \begin{pmatrix} (\natural)_{11} & 0 & 0 & \frac{1}{2} \lambda_{H\Phi} h_{2c} \phi_{Hc} \\ 0 & (\natural)_{22} & 0 & -\frac{1}{2} \lambda'_{H\Phi} h_{1c} \phi_{Hc} \\ 0 & 0 & (\natural)_{22} & \frac{1}{2} \lambda'_{H\Phi} h_{1c} h_{2c} \\ \frac{1}{2} \lambda_{H\Phi} h_{2c} \phi_{Hc} & -\frac{1}{2} \lambda'_{H\Phi} h_{1c} \phi_{Hc} & \frac{1}{2} \lambda'_{H\Phi} h_{1c} h_{2c} & (\natural)_{44} \end{pmatrix}, \quad (\text{A18})$$

with the following diagonal elements

$$(\mathfrak{h})_{11} = -\mu_H^2 + \lambda_H h_+^2 + \frac{1}{2} \lambda_{H\Phi} \phi_{Hc}^2, \quad (\text{A19})$$

$$(\mathfrak{h})_{22} = -\mu_H^2 + \lambda_H h_+^2 + \frac{1}{2} \tilde{\lambda}_{H\Phi} \phi_{Hc}^2, \quad (\text{A20})$$

$$(\mathfrak{h})_{33} = -\mu_\Phi^2 + \lambda_\Phi \phi_{Hc}^2 + \frac{1}{2} (\lambda_{H\Phi} h_+^2 + \lambda'_{H\Phi} h_{2c}^2), \quad (\text{A21})$$

$$(\mathfrak{h})_{44} = -\mu_\Phi^2 + \lambda_\Phi \phi_{Hc}^2 + \frac{1}{2} (\lambda_{H\Phi} h_+^2 + \lambda'_{H\Phi} h_{1c}^2). \quad (\text{A22})$$

Similarly, including the thermal masses, we have

$$\overline{M}_P^2 = M_P^2 + \begin{pmatrix} \Pi_{H_1}(T) & 0 & 0 & 0 \\ 0 & \Pi_{H_2}(T) & 0 & 0 \\ 0 & 0 & \Pi_{\Phi_H}(T) & 0 \\ 0 & 0 & 0 & \Pi_{\Phi_H}(T) \end{pmatrix}. \quad (\text{A23})$$

We denote the eigenvalues of M_P^2 and \overline{M}_P^2 as $m_{P_i}^2$ and $\overline{m}_{P_i}^2$ respectively for the CP-odd states P_i with $i = 1, 2, 3$, and 4.

Since the matrix elements of $M_S^2(\overline{M}_S^2)$ and $M_P^2(\overline{M}_P^2)$ depend on the values of μ_H^2 and μ_Φ^2 , the scalar mass spectrum depends on the detail of the symmetry breaking patterns just like the gauge bosons. Similarly one can reproduce the zero temperature mass spectra and mixings for the scalars presented in Sec. [II B](#) by ignoring the thermal masses and setting $h_{1c} \rightarrow v$, $h_{2c} \rightarrow 0$ and $\phi_{Hc} \rightarrow v_\Phi$ in the above formulae. For example, G_H^1 and G_H^2 will have the same mass and they can be combined into two complex Goldstone bosons $G_H^{(p,m)} = (G_H^1 \pm iG_H^2)/\sqrt{2}$ absorbed by the longitudinal components of $W'^{(p,m)}$, and h_{SM} and ϕ_H can be combined into h_1 and h_2 , and so on.

3. Fermions

The gauge invariant Yukawa couplings in G2HDM lead to the following fermionic mass terms in the Lagrangian [148]

$$\begin{aligned}
\mathcal{L}_{\text{mass}}^f &= -\frac{1}{\sqrt{2}} (\bar{u}_L, \bar{u}_L^H) \begin{pmatrix} v_1 \mathcal{Y}_u & v_2 \mathcal{Y}_u \\ 0 & v_\Phi \mathcal{Y}'_u \end{pmatrix} \begin{pmatrix} u_R \\ u_R^H \end{pmatrix} + \text{H.c.} \\
&- \frac{1}{\sqrt{2}} (\bar{d}_L, \bar{d}_L^H) \begin{pmatrix} v_1 \mathcal{Y}_d & -v_2 \mathcal{Y}_d \\ 0 & v_\Phi \mathcal{Y}'_d \end{pmatrix} \begin{pmatrix} d_R \\ d_R^H \end{pmatrix} + \text{H.c.} \\
&- \frac{1}{\sqrt{2}} (\bar{\nu}_L, \bar{\nu}_L^H) \begin{pmatrix} v_1 \mathcal{Y}_\nu & v_2 \mathcal{Y}_\nu \\ 0 & v_\Phi \mathcal{Y}'_\nu \end{pmatrix} \begin{pmatrix} \nu_R \\ \nu_R^H \end{pmatrix} + \text{H.c.} \\
&- \frac{1}{\sqrt{2}} (\bar{e}_L, \bar{e}_L^H) \begin{pmatrix} v_1 \mathcal{Y}_e & -v_2 \mathcal{Y}_e \\ 0 & v_\Phi \mathcal{Y}'_e \end{pmatrix} \begin{pmatrix} e_R \\ e_R^H \end{pmatrix} + \text{H.c.} \quad (\text{A24})
\end{aligned}$$

Since the lower left blocks in the mass matrices vanish, the SM fermions f_R will not mix with the hidden fermions f_L^H in G2HDM even if $v_2 \neq 0$. The Yukawa matrices \mathcal{Y}_f and \mathcal{Y}'_f can be blocked diagonalized independently. Since fermion loops do not suffer from the infrared problems associated with the zero Matsubara frequencies in the bosonic case, daisy resummation is not necessary. The leading temperature effects for the fermion masses are usually captured via the following prescriptions

$$m_f^2(v_1) = \frac{1}{2} y_f^2 v_1^2 \rightarrow m_f^2(h_{1c}) = \frac{1}{2} y_f^2 h_{1c}(T)^2 = m_f^2(v_1) \frac{h_{1c}(T)^2}{v_1^2}, \quad (\text{A25})$$

$$m_{fH}^2(v_\Phi) = \frac{1}{2} y_{fH}^2 v_\Phi^2 \rightarrow m_{fH}^2(\phi_{Hc}) = \frac{1}{2} y_{fH}^2 \phi_{Hc}(T)^2 = m_{fH}^2(v_\Phi) \frac{\phi_{Hc}(T)^2}{v_\Phi^2}, \quad (\text{A26})$$

where y_f^2 and y_{fH}^2 are the eigenvalues of the Yukawa matrices $\mathcal{Y}_f \mathcal{Y}_f^\dagger$ (or $\mathcal{Y}_f^\dagger \mathcal{Y}_f$) and $\mathcal{Y}'_f \mathcal{Y}'_f^\dagger$ (or $\mathcal{Y}'_f^\dagger \mathcal{Y}'_f$) respectively. The temperature dependence for the fermion masses are coming through the classical fields $h_{1c}(T)$ and $\phi_{Hc}(T)$ only. For simplicity, we will consider just the heavy top quark t and its hidden heavy partner t^H from the third generation in the numerical work since they represent the most dominant contribution from the fermion sector.

Appendix B: Thermal Masses

In this appendix, we list the thermal mass (Debye screening mass) for all the scalar and vector bosons in G2HDM. Including these masses are essential for the resummation of the daisy diagrams in the finite temperature effective potential.

For the two doublets H_1 and H_2 , using the field components defined in Eq. (3), we found

$$\begin{aligned}\Pi_{H_1}(T) &\equiv \Pi_{h_1}(T) = \Pi_{G_1^0}(T) = \Pi_{h_1^\pm}(T) = \tilde{\Pi}_{H_1} T^2 \\ &= \frac{1}{12} (10\lambda_H - \lambda'_H + 2\lambda_{H\Phi} + \lambda'_{H\Phi}) T^2 \\ &\quad + \frac{1}{16} (3g^2 + g'^2 + 3g_H^2 + g_X^2) T^2 + \frac{1}{4} y_t^2 T^2 ,\end{aligned}\tag{B1}$$

$$\begin{aligned}\Pi_{H_2}(T) &\equiv \Pi_{h_2}(T) = \Pi_{G_2^0}(T) = \Pi_{h_2^\pm}(T) = \tilde{\Pi}_{H_2} T^2 \\ &= \frac{1}{12} (10\lambda_H - \lambda'_H + 2\lambda_{H\Phi} + \lambda'_{H\Phi}) T^2 \\ &\quad + \frac{1}{16} (3g^2 + g'^2 + 3g_H^2 + g_X^2) T^2 ,\end{aligned}\tag{B2}$$

and for the hidden doublet Φ_H , using Eq. (4), we got

$$\begin{aligned}\Pi_{\Phi_H}(T) &\equiv \Pi_{\phi_H}(T) = \Pi_{G_H^0}(T) = \Pi_{G_H^{(p,m)}}(T) = \tilde{\Pi}_{\Phi_H} T^2 \\ &= \frac{1}{6} (3\lambda_\Phi + 2\lambda_{H\Phi} + \lambda'_{H\Phi}) T^2 + \frac{1}{16} (3g_H^2 + g_X^2) T^2 + \frac{1}{4} y_t^2 T^2 .\end{aligned}\tag{B3}$$

For the Yukawa couplings, we will keep only the contributions from the SM top quark (y_t) and its heavy partner (y'_t) in G2HDM.

For the SM gauge bosons, we have

$$\Pi_W(T) \equiv \Pi_{W^i}(T) = 2g^2 T^2 , \quad (i = 1, 2, 3)\tag{B4}$$

$$\Pi_B(T) = \frac{14}{3} g'^2 T^2 .\tag{B5}$$

For the hidden gauge bosons, we have

$$\Pi_{W'}(T) \equiv \Pi_{W'^i}(T) = \frac{19}{6} g_H^2 T^2 , \quad (i = 1, 2, 3)\tag{B6}$$

$$\Pi_X(T) = \frac{17}{2} g_X^2 T^2 .\tag{B7}$$

In the thermal masses of the gauge bosons, we have summed over all three generations of quarks and leptons in G2HDM.

Appendix C: Thermal Integrals

The definition of $J_i(x)$ depends on whether i is a boson (B) or a fermion (F), *i.e.*

$$J_{B/F}(x) \equiv \int_0^\infty dy y^2 \log \left[1 \mp \exp \left(-\sqrt{x^2 + y^2} \right) \right]. \quad (\text{C1})$$

Note that in our notation, $x \equiv m_{B/F}/T$. In the literature, some authors' x is our x^2 .

For high-T where $x \ll 1$, one has the following series expansions [247]

$$J_B(x) = -\frac{\pi^4}{45} + \frac{\pi^2}{12}x^2 - \frac{\pi}{6}(x^2)^{3/2} - \frac{1}{32}x^4 \log \left(\frac{x^2}{c_B} \right) - \frac{1}{8\pi^{1/2}}x^4 \sum_{l=1}^{\infty} (-1)^l \frac{\zeta(2l+1)}{(l+1)!} \Gamma \left(l + \frac{1}{2} \right) \left(\frac{x^2}{4\pi^2} \right)^l, \quad (\text{C2})$$

$$J_F(x) = \frac{7}{8} \cdot \frac{\pi^4}{45} - \frac{\pi^2}{24}x^2 - \frac{1}{32}x^4 \log \left(\frac{x^2}{c_F} \right) - \frac{1}{4\pi^{1/2}}x^4 \sum_{l=1}^{\infty} (-1)^l \left(1 - \frac{1}{2^{2l+1}} \right) \frac{\zeta(2l+1)}{(l+1)!} \Gamma \left(l + \frac{1}{2} \right) \left(\frac{x^2}{\pi^2} \right)^l, \quad (\text{C3})$$

where $c_B = 16\pi^2 \exp \left(\frac{3}{2} - 2\gamma_E \right)$, $c_F = c_B/16$, and $\Gamma(z)$ and $\zeta(z)$ are the Euler Γ -function and Riemann ζ -function respectively. Numerically, we have

$$\begin{aligned} \gamma_E &= 0.5772156649015329 \dots, \\ c_B &= 223.0993446886696 \dots, \\ c_F &= 13.94370904304185 \dots. \end{aligned} \quad (\text{C4})$$

Note that there is no $(x^2)^{3/2}$ term in J_F ! For high-T, keeping the first lines in (C2) and (C3) are usually sufficient!

On the other hand, we also have the following series representations [248]

$$J_B(x) = - \sum_{n=1}^{\infty} \frac{1}{n^2} x^2 K_2(nx) , \quad (\text{C5})$$

$$J_F(x) = - \sum_{n=1}^{\infty} \frac{1}{n^2} (-1)^n x^2 K_2(nx) , \quad (\text{C6})$$

where $K_2(z)$ is the modified Bessel function of second kind which falls off exponentially for large positive values of z . For high mass or low temperature where $x \gg 1$, these series representations converge rapidly. Usually, taking the first five terms in the series is sufficient [67, 129].

The thermal integral $\mathcal{J}_i(x_i)$ in (33) is defined by [204, 205]

$$\mathcal{J}_i \left(\frac{m_i}{T} \right) = \begin{cases} J_B \left(\frac{m_i}{T} \right) - \frac{\pi}{6} \left(\frac{\bar{m}_i^3}{T^3} - \frac{m_i^3}{T^3} \right) , & i \in \{S_1, S_2, S_3, S_4, P_1, P_2, P_3, P_4, G^\pm, H^\pm \\ & W_L^\pm, W_L'^2, Z_{1L}, Z_{2L}, Z_{3L}, Z_{4L}, \gamma_L\} ; \\ J_B \left(\frac{m_i}{T} \right) , & i \in \{W_T^\pm, W_T'^2, Z_{1T}, Z_{2T}, Z_{3T}, Z_{4T}, \gamma_T\} ; \\ J_F \left(\frac{m_i}{T} \right) , & i \in \{l, \nu, l^H, \nu^H, q, q^H\} . \end{cases} \quad (\text{C7})$$

Note that for the scalars and longitudinal components of the gauge bosons we have included the resummation effects from the daisy (ring) diagrams from higher loops in the thermal corrections. \bar{m}_i and m_i are the field dependent masses (mass eigenvalues in case of mixings) with and without the thermal mass correction respectively for particle i .

It has been shown recently [183] that at high-T the daisy resummation can be quite poor for large values of the quartic coupling in BSM and does not shown how decoupling occurs when the internal mass of the BSM particle is large compared with the temperature. More accurate calculation would have to include the superdaisy diagrams which will lead one to solve the gap equations [183]. We will not get into this business here. Also ignored here is the two-loop corrections to the finite temperature effective potential which have been shown quite relevant to determine the strength of the phase transition in MSSM [249].

Appendix D: Gauge-Invariant Method Beyond Leading Order and Scale Dependence

The determination of the phase transition quantities such as v_C and T_C in a gauge theory can lead to the gauge fixing parameter dependence if the effective potential is calculated beyond the leading high-T approximation. However one can treat the gauge dependence issue using the \hbar -expansion method proposed in Ref.[145]. Such method is based on the Nielsen-Fukuda-Kugo (NFK) identity [187, 188], which states that the energies at the stationary points of the effective potential are independent of the gauge fixing parameter ξ . The NFK identity can be described by

$$\frac{\partial V_{\text{eff}}(\varphi)}{\partial \xi} = -C(\varphi, \xi) \frac{\partial V_{\text{eff}}(\varphi)}{\partial \varphi}, \quad (\text{D1})$$

where the functional $C(\varphi, \xi)$ can be found explicitly in Ref. [187].

By expanding both the effective potential and the functional $C(\varphi, \xi)$ in powers of \hbar ,

$$V_{\text{eff}}(\varphi) = V_0(\varphi) + \hbar V_1(\varphi) + \hbar^2 V_2(\varphi) + \dots, \quad (\text{D2})$$

$$C(\varphi, \xi) = c_0 + \hbar c_1(\varphi) + \hbar^2 c_2(\varphi) + \dots, \quad (\text{D3})$$

and, for example, considering the first order with respect to \hbar , one can obtain from (D1)

$$\frac{\partial V_1}{\partial \xi} = -c_1 \frac{\partial V_0}{\partial \varphi}, \quad (\text{D4})$$

which implies that the ξ -dependence of V_1 can be eliminated at the extremal points of the tree-level potential. Therefore, the critical temperature to $\mathcal{O}(\hbar)$ can be determined by evaluating the degeneracy condition of the effective potential at the stationary points of the tree-level potential. For the transition from the $(0, h_{2c}, 0)$ phase to $(h_{1c}, 0, \phi_{Hc})$ phase in G2HDM as depicted in the right panel of

Fig. 1 where $s \equiv \phi_{Hc}$, $h_1 \equiv h_{1c}$ and $h_2 \equiv h_{2c}$, the critical temperature T_C can be determined by solving the following equation

$$V_0(0, v_2, 0) + V_1(0, v_2, 0, T_C) = V_0(v_1, 0, v_\Phi) + V_1(v_1, 0, v_\Phi, T_C) , \quad (\text{D5})$$

where $(0, v_2, 0)$ and $(v_1, 0, v_\Phi)$ are the extremal points at the tree-level potential. On the other hand, the value of v_C is determined by utilizing the high-T expansion effective potential.

Another issue that arises in the calculation beyond the high-T expansion effective potential is the dependence on the renormalization scale μ in the Coleman-Weinberg effective potential V_{CW} . This dependence can have a significant impact on the properties of phase transitions and the associated predicted GW signals [189, 190]. To mitigate this dependence, renormalization group (RG) improvement can be applied to the effective potential [250–254]. This can be done by running the parameters in the tree-level effective potential using the β functions given in Appendix F. At leading order, the RG improved potential satisfies

$$\mu \frac{d}{d\mu} [V_0(\mu) + V_{\text{CW}}(\mu)] = 0 , \quad (\text{D6})$$

which ensures independence from the choice of μ .

Appendix E: The Critical Temperatures

In this section, we show the analytical expressions for the critical temperatures in the two-step phase transition. The critical temperature for the first step $[(0, 0, 0) \rightarrow (0, h_{2c}, 0)]$ can be easily obtained by solving the degenerate condition $V_{\text{eff}}^{\text{HT}}(0, 0, 0, T_{1C}) = V_{\text{eff}}^{\text{HT}}(0, h_{2c}, 0, T_{1C})$. This gives the result of

$$T_{1C} = \sqrt{\mu_H^2 / \tilde{\Pi}_{H_2}}, \quad (\text{E1})$$

where $\mu_H^2 = \lambda_H v^2 + \lambda_{H\Phi} v_\Phi^2 / 2$ fixed by the tree level tadpole condition and $\tilde{\Pi}_{H_2}$ is given by (39).

For the second step $[(0, h_{2c}, 0) \rightarrow (h_{1c}, 0, \phi_{Hc})]$, by solving the following degenerate condition

$$V_{\text{eff}}^{\text{HT}}(0, h_{2c}, 0, T_C) = V_{\text{eff}}^{\text{HT}}(h_{1c}, 0, \phi_{Hc}, T_C), \quad (\text{E2})$$

one obtains

$$T_C = \sqrt{\frac{(\lambda_{H\Phi}^2 - 4\lambda_H \lambda_\Phi) v_\Phi^4}{2 \left(\lambda_{H\Phi} \tilde{\Pi}_{H_2} - 2\lambda_H \tilde{\Pi}_{\Phi_H} \right) v_\Phi^2 - \lambda_H y_t^2 v^2 - \kappa}}, \quad (\text{E3})$$

where

$$\begin{aligned} \kappa = y_t \lambda_H^{1/2} \left\{ \left[4\lambda_{H\Phi} \tilde{\Pi}_{\Phi_H} - \lambda_\Phi (8\tilde{\Pi}_{H_2} + y_t^2) \right] v_\Phi^4 \right. \\ \left. + 4 \left(2\lambda_H \tilde{\Pi}_{\Phi_H} - \lambda_{H\Phi} \tilde{\Pi}_{H_2} \right) v^2 v_\Phi^2 + \lambda_H y_t^2 v^4 \right\}^{1/2}, \end{aligned} \quad (\text{E4})$$

$$\tilde{\Pi}_{\Phi_H} = \frac{1}{6} (3\lambda_\Phi + 2\lambda_{H\Phi} + \lambda'_{H\Phi}) + \frac{1}{16} (3g_H^2 + g_X^2) + \frac{1}{4} y_t'^2. \quad (\text{E5})$$

We note that with the viable parameter space in the model, the critical temperature T_C stays in the electroweak scale as shown in Fig. 6.

Appendix F: Renormalization Group Equations

Here we present the one loop renormalization group equations in G2HDM. The β -function, computed with the help of SARAH [255], is defined as $\beta_X \equiv \mu dX/d\mu$, where X denotes a generic coupling/mass and μ is the renormalization scale.

Gauge couplings:

$$\beta_{g'} = \frac{1}{16\pi^2} \left(\frac{53}{3} g'^3 \right), \quad (\text{F1})$$

$$\beta_g = \frac{1}{16\pi^2} (-3g^3), \quad (\text{F2})$$

$$\beta_{g_s} = \frac{1}{16\pi^2} (-3g_s^3), \quad (\text{F3})$$

$$\beta_{g_X} = \frac{1}{16\pi^2} \left(\frac{17}{2} g_X^3 \right), \quad (\text{F4})$$

$$\beta_{g_H} = \frac{1}{16\pi^2} \left(\frac{7}{6} g_H^3 \right). \quad (\text{F5})$$

Scalar masses and quartic couplings:

$$\begin{aligned} \beta_{\mu_H^2} = & \frac{1}{16\pi^2} \left[4\mu_H^2 \left(5\lambda_H - \frac{1}{2}\lambda'_H \right) - \frac{3}{2}\mu_H^2 (3g^2 + g'^2 + 3g_H^2 + g_X^2 - 4y_t^2) \right. \\ & \left. + 2\mu_\Phi^2 (2\lambda_{H\Phi} + \lambda'_{H\Phi}) \right], \end{aligned} \quad (\text{F6})$$

$$\beta_{\mu_\Phi^2} = \frac{1}{16\pi^2} \left[12\mu_\Phi^2 \lambda_\Phi - \frac{3}{2}\mu_\Phi^2 (3g_H^2 + g_X^2 - 4y_{tH}^2) + 4\mu_H^2 (2\lambda_{H\Phi} + \lambda'_{H\Phi}) \right], \quad (\text{F7})$$

$$\begin{aligned} \beta_{\lambda_H} = & \frac{1}{16\pi^2} \left\{ 32\lambda_H^2 + \lambda_H'^2 + 2\lambda_{H\Phi}^2 + \lambda_{H\Phi}'^2 - 4\lambda_H \lambda_H' + 2\lambda_{H\Phi} \lambda_{H\Phi}' \right. \\ & - 3\lambda_H (3g^2 + g'^2 + 3g_H^2 + g_X^2) \\ & \left. + \frac{3}{8} \left[g^4 + 3g_H^4 + 2g_H^2 (g'^2 + g_X^2) + (g'^2 + g_X^2)^2 + 2g^2 (g'^2 + g_H^2 + g_X^2) \right] \right. \\ & \left. + 6y_t^2 (2\lambda_H - y_t^2) \right\}, \end{aligned} \quad (\text{F8})$$

$$\begin{aligned} \beta_{\lambda_H'} = & \frac{1}{16\pi^2} \left[2(2\lambda_H'^2 - \lambda_{H\Phi}'^2 + 12\lambda_H \lambda_H') - 3\lambda_H' (3g^2 + g'^2 + 3g_H^2 + g_X^2) \right. \\ & \left. + 3g_H^2 (2g^2 - g'^2 - g_X^2) - 3g^2 (g'^2 + g_X^2) + 12(2\lambda_H + 3\lambda_H') y_t^2 \right], \end{aligned} \quad (\text{F9})$$

$$\beta_{\lambda_\Phi} = \frac{1}{16\pi^2} \left[4 \left(6\lambda_\Phi^2 + \lambda_{H\Phi}^2 + \lambda_{H\Phi}\lambda'_{H\Phi} + \frac{1}{2}\lambda_{H\Phi}^{\prime 2} \right) - 3\lambda_\Phi (3g_H^2 + g_X^2) + \frac{3}{8} (3g_H^4 + g_X^4 + 2g_H^2 g_X^2) + 6y_{tH}^2 (2\lambda_\Phi - y_{tH}^2) \right], \quad (\text{F10})$$

$$\beta_{\lambda_{H\Phi}} = \frac{1}{16\pi^2} \left[2 \left(10\lambda_H\lambda_{H\Phi} + 2\lambda_{H\Phi}^2 + 4\lambda_H\lambda'_{H\Phi} + \lambda_{H\Phi}^{\prime 2} - \lambda_H\lambda'_H - \lambda'_{H\Phi}\lambda'_H + 6\lambda_{H\Phi}\lambda_\Phi + 2\lambda'_{H\Phi}\lambda_\Phi \right) - \frac{3}{2} (g'^2 + 3g^2 + 6g_H^2 + 2g_X^2) \lambda_{H\Phi} + \frac{3}{4} (3g_H^4 + g_X^4 - 2g_H^2 g_X^2) + 6\lambda_{H\Phi} (y_t^2 + y_{tH}^2) \right], \quad (\text{F11})$$

$$\beta_{\lambda'_{H\Phi}} = \frac{1}{16\pi^2} \left[2\lambda'_{H\Phi} (2\lambda'_{H\Phi} + 2\lambda_H + \lambda'_H + 2\lambda_\Phi + 4\lambda_{H\Phi}) - \frac{3}{2} (3g^2 + 6g_H^2 + g'^2 + 2g_X^2) \lambda'_{H\Phi} + 3g_H^2 g_X^2 + 6\lambda'_{H\Phi} (y_t^2 + y_{tH}^2) \right]. \quad (\text{F12})$$

Yukawa couplings:

$$\beta_{y_t} = \frac{1}{16\pi^2} \left[18y_t^3 - y_t \left(-2y_{tH}^2 + \frac{17}{2}g_s^2 + \frac{9}{4}g^2 + \frac{17}{12}g'^2 + \frac{9}{4}g_H^2 + \frac{3}{4}g_X^2 \right) \right], \quad (\text{F13})$$

$$\beta_{y_{tH}} = \frac{1}{16\pi^2} \left[16y_{tH}^3 - y_{tH} \left(-4y_t^2 + \frac{17}{2}g_s^2 + \frac{8}{3}g'^2 + \frac{9}{4}g_H^2 + \frac{3}{4}g_X^2 \right) \right]. \quad (\text{F14})$$

-
- [1] K. Kajantie, M. Laine, K. Rummukainen, and M. E. Shaposhnikov, *Phys. Rev. Lett.* **77**, 2887 (1996), [arXiv:hep-ph/9605288](#).
- [2] K. Rummukainen, M. Tsypin, K. Kajantie, M. Laine, and M. E. Shaposhnikov, *Nucl. Phys. B* **532**, 283 (1998), [arXiv:hep-lat/9805013](#).
- [3] M. Laine and K. Rummukainen, *Nucl. Phys. B Proc. Suppl.* **73**, 180 (1999), [arXiv:hep-lat/9809045](#).
- [4] Y. Aoki, F. Csikor, Z. Fodor, and A. Ukawa, *Phys. Rev. D* **60**, 013001 (1999), [arXiv:hep-lat/9901021](#).
- [5] J. McDonald, *Phys. Lett. B* **323**, 339 (1994).
- [6] S. Profumo, M. J. Ramsey-Musolf, and G. Shaughnessy, *JHEP* **08**, 010 (2007), [arXiv:0705.2425 \[hep-ph\]](#).
- [7] J. M. Cline, G. Laporte, H. Yamashita, and S. Kraml, *JHEP* **07**, 040 (2009), [arXiv:0905.2559 \[hep-ph\]](#).
- [8] J. R. Espinosa, T. Konstandin, and F. Riva, *Nucl. Phys. B* **854**, 592 (2012), [arXiv:1107.5441 \[hep-ph\]](#).
- [9] J. M. Cline and K. Kainulainen, *JCAP* **01**, 012 (2013), [arXiv:1210.4196 \[hep-ph\]](#).
- [10] T. Alanne, K. Tuominen, and V. Vaskonen, *Nucl. Phys. B* **889**, 692 (2014), [arXiv:1407.0688 \[hep-ph\]](#).
- [11] D. Curtin, P. Meade, and C.-T. Yu, *JHEP* **11**, 127 (2014), [arXiv:1409.0005 \[hep-ph\]](#).
- [12] S. Profumo, M. J. Ramsey-Musolf, C. L. Wainwright, and P. Winslow, *Phys. Rev. D* **91**, 035018 (2015), [arXiv:1407.5342 \[hep-ph\]](#).
- [13] F. P. Huang and C. S. Li, *Phys. Rev. D* **92**, 075014 (2015), [arXiv:1507.08168 \[hep-ph\]](#).
- [14] A. V. Kotwal, M. J. Ramsey-Musolf, J. M. No, and P. Winslow, *Phys. Rev. D* **94**,

- 035022 (2016), [arXiv:1605.06123 \[hep-ph\]](#).
- [15] V. Vaskonen, *Phys. Rev. D* **95**, 123515 (2017), [arXiv:1611.02073 \[hep-ph\]](#).
- [16] P. H. Ghorbani, *JHEP* **08**, 058 (2017), [arXiv:1703.06506 \[hep-ph\]](#).
- [17] J. M. Cline, K. Kainulainen, and D. Tucker-Smith, *Phys. Rev. D* **95**, 115006 (2017), [arXiv:1702.08909 \[hep-ph\]](#).
- [18] A. Beniwal, M. Lewicki, J. D. Wells, M. White, and A. G. Williams, *JHEP* **08**, 108 (2017), [arXiv:1702.06124 \[hep-ph\]](#).
- [19] G. Kurup and M. Perelstein, *Phys. Rev. D* **96**, 015036 (2017), [arXiv:1704.03381 \[hep-ph\]](#).
- [20] C.-W. Chiang, M. J. Ramsey-Musolf, and E. Senaha, *Phys. Rev. D* **97**, 015005 (2018), [arXiv:1707.09960 \[hep-ph\]](#).
- [21] M. Carena, M. Quirós, and Y. Zhang, *Phys. Rev. Lett.* **122**, 201802 (2019), [arXiv:1811.09719 \[hep-ph\]](#).
- [22] M. Carena, Z. Liu, and M. Riembau, *Phys. Rev. D* **97**, 095032 (2018), [arXiv:1801.00794 \[hep-ph\]](#).
- [23] B. Grzadkowski and D. Huang, *JHEP* **08**, 135 (2018), [arXiv:1807.06987 \[hep-ph\]](#).
- [24] F. P. Huang, Z. Qian, and M. Zhang, *Phys. Rev. D* **98**, 015014 (2018), [arXiv:1804.06813 \[hep-ph\]](#).
- [25] A. Alves, T. Ghosh, H.-K. Guo, K. Sinha, and D. Vagie, *JHEP* **04**, 052 (2019), [arXiv:1812.09333 \[hep-ph\]](#).
- [26] K. Ghorbani and P. H. Ghorbani, *J. Phys. G* **47**, 015201 (2020), [arXiv:1804.05798 \[hep-ph\]](#).
- [27] W. Cheng and L. Bian, *Phys. Rev. D* **98**, 023524 (2018), [arXiv:1801.00662 \[hep-ph\]](#).
- [28] T. Alanne, T. Hugle, M. Platscher, and K. Schmitz, *JHEP* **03**, 004 (2020), [arXiv:1909.11356 \[hep-ph\]](#).
- [29] O. Gould, J. Kozaczuk, L. Niemi, M. J. Ramsey-Musolf, T. V. I. Tenkanen, and D. J. Weir, *Phys. Rev. D* **100**, 115024 (2019), [arXiv:1903.11604 \[hep-ph\]](#).

- [30] M. Carena, Z. Liu, and Y. Wang, *JHEP* **08**, 107 (2020), [arXiv:1911.10206 \[hep-ph\]](#).
- [31] H.-L. Li, M. Ramsey-Musolf, and S. Willocq, *Phys. Rev. D* **100**, 075035 (2019), [arXiv:1906.05289 \[hep-ph\]](#).
- [32] N. F. Bell, M. J. Dolan, L. S. Friedrich, M. J. Ramsey-Musolf, and R. R. Volkas, *JHEP* **09**, 012 (2019), [arXiv:1903.11255 \[hep-ph\]](#).
- [33] S. Inoue, G. Ovanesyan, and M. J. Ramsey-Musolf, *Phys. Rev. D* **93**, 015013 (2016), [arXiv:1508.05404 \[hep-ph\]](#).
- [34] L. Niemi, H. H. Patel, M. J. Ramsey-Musolf, T. V. I. Tenkanen, and D. J. Weir, *Phys. Rev. D* **100**, 035002 (2019), [arXiv:1802.10500 \[hep-ph\]](#).
- [35] M. Chala, M. Ramos, and M. Spannowsky, *Eur. Phys. J. C* **79**, 156 (2019), [arXiv:1812.01901 \[hep-ph\]](#).
- [36] R. Zhou, W. Cheng, X. Deng, L. Bian, and Y. Wu, *JHEP* **01**, 216 (2019), [arXiv:1812.06217 \[hep-ph\]](#).
- [37] A. I. Bochkev, S. V. Kuzmin, and M. E. Shaposhnikov, *Phys. Lett. B* **244**, 275 (1990).
- [38] L. D. McLerran, M. E. Shaposhnikov, N. Turok, and M. B. Voloshin, *Phys. Lett. B* **256**, 451 (1991).
- [39] A. I. Bochkev, S. V. Kuzmin, and M. E. Shaposhnikov, *Phys. Rev. D* **43**, 369 (1991).
- [40] N. Turok and J. Zadrozny, *Nucl. Phys. B* **358**, 471 (1991).
- [41] A. G. Cohen, D. B. Kaplan, and A. E. Nelson, *Phys. Lett. B* **263**, 86 (1991).
- [42] N. Turok and J. Zadrozny, *Nucl. Phys. B* **369**, 729 (1992).
- [43] A. E. Nelson, D. B. Kaplan, and A. G. Cohen, *Nucl. Phys. B* **373**, 453 (1992).
- [44] K. Funakubo, A. Kakuto, and K. Takenaga, *Prog. Theor. Phys.* **91**, 341 (1994), [arXiv:hep-ph/9310267](#).
- [45] A. T. Davies, C. D. Froggatt, G. Jenkins, and R. G. Moorhouse, *Phys. Lett. B* **336**, 464 (1994).

- [46] J. M. Cline, K. Kainulainen, and A. P. Vischer, *Phys. Rev. D* **54**, 2451 (1996), [arXiv:hep-ph/9506284](#).
- [47] K. Funakubo, A. Kakuto, S. Otsuki, K. Takenaga, and F. Toyoda, *Prog. Theor. Phys.* **94**, 845 (1995), [arXiv:hep-ph/9507452](#).
- [48] K. Funakubo, A. Kakuto, S. Otsuki, and F. Toyoda, *Prog. Theor. Phys.* **96**, 771 (1996), [arXiv:hep-ph/9606282](#).
- [49] J. M. Cline and P.-A. Lemieux, *Phys. Rev. D* **55**, 3873 (1997), [arXiv:hep-ph/9609240](#).
- [50] L. Fromme, S. J. Huber, and M. Seniuch, *JHEP* **11**, 038 (2006), [arXiv:hep-ph/0605242](#).
- [51] J. M. Cline, K. Kainulainen, and M. Trott, *JHEP* **11**, 089 (2011), [arXiv:1107.3559 \[hep-ph\]](#).
- [52] G. C. Dorsch, S. J. Huber, and J. M. No, *JHEP* **10**, 029 (2013), [arXiv:1305.6610 \[hep-ph\]](#).
- [53] J. M. Cline and K. Kainulainen, *Phys. Rev. D* **87**, 071701 (2013), [arXiv:1302.2614 \[hep-ph\]](#).
- [54] G. C. Dorsch, S. J. Huber, K. Mimasu, and J. M. No, *Phys. Rev. Lett.* **113**, 211802 (2014), [arXiv:1405.5537 \[hep-ph\]](#).
- [55] K. Fuyuto and E. Senaha, *Phys. Lett. B* **747**, 152 (2015), [arXiv:1504.04291 \[hep-ph\]](#).
- [56] W. Chao and M. J. Ramsey-Musolf, (2015), [arXiv:1503.00028 \[hep-ph\]](#).
- [57] K. Fuyuto, J. Hisano, and E. Senaha, *Phys. Lett. B* **755**, 491 (2016), [arXiv:1510.04485 \[hep-ph\]](#).
- [58] C.-W. Chiang, K. Fuyuto, and E. Senaha, *Phys. Lett. B* **762**, 315 (2016), [arXiv:1607.07316 \[hep-ph\]](#).
- [59] A. Haarr, A. Kvellestad, and T. C. Petersen, (2016), [arXiv:1611.05757 \[hep-ph\]](#).
- [60] G. C. Dorsch, S. J. Huber, T. Konstandin, and J. M. No, *JCAP* **05**, 052 (2017),

- [arXiv:1611.05874 \[hep-ph\]](#).
- [61] P. Basler, M. Krause, M. Muhlleitner, J. Wittbrodt, and A. Wlotzka, *JHEP* **02**, 121 (2017), [arXiv:1612.04086 \[hep-ph\]](#).
 - [62] K. Fuyuto, W.-S. Hou, and E. Senaha, *Phys. Lett. B* **776**, 402 (2018), [arXiv:1705.05034 \[hep-ph\]](#).
 - [63] G. C. Dorsch, S. J. Huber, K. Mimasu, and J. M. No, *JHEP* **12**, 086 (2017), [arXiv:1705.09186 \[hep-ph\]](#).
 - [64] A. L. Cherchiglia and C. C. Nishi, *JHEP* **11**, 106 (2017), [arXiv:1707.04595 \[hep-ph\]](#).
 - [65] P. Basler, M. Mühlleitner, and J. Wittbrodt, *JHEP* **03**, 061 (2018), [arXiv:1711.04097 \[hep-ph\]](#).
 - [66] J. O. Andersen, T. Gorda, A. Helset, L. Niemi, T. V. I. Tenkanen, A. Tranberg, A. Vuorinen, and D. J. Weir, *Phys. Rev. Lett.* **121**, 191802 (2018), [arXiv:1711.09849 \[hep-ph\]](#).
 - [67] J. Bernon, L. Bian, and Y. Jiang, *JHEP* **05**, 151 (2018), [arXiv:1712.08430 \[hep-ph\]](#).
 - [68] F. P. Huang and J.-H. Yu, *Phys. Rev. D* **98**, 095022 (2018), [arXiv:1704.04201 \[hep-ph\]](#).
 - [69] T. Gorda, A. Helset, L. Niemi, T. V. I. Tenkanen, and D. J. Weir, *JHEP* **02**, 081 (2019), [arXiv:1802.05056 \[hep-ph\]](#).
 - [70] P. Basler and M. Mühlleitner, *Comput. Phys. Commun.* **237**, 62 (2019), [arXiv:1803.02846 \[hep-ph\]](#).
 - [71] T. Modak and E. Senaha, *Phys. Rev. D* **99**, 115022 (2019), [arXiv:1811.08088 \[hep-ph\]](#).
 - [72] L. Wang, J. M. Yang, M. Zhang, and Y. Zhang, *Phys. Lett. B* **788**, 519 (2019), [arXiv:1809.05857 \[hep-ph\]](#).
 - [73] X. Wang, F. P. Huang, and X. Zhang, *Phys. Rev. D* **101**, 015015 (2020), [arXiv:1909.02978 \[hep-ph\]](#).
 - [74] K. Kainulainen, V. Keus, L. Niemi, K. Rummukainen, T. V. I. Tenkanen, and

- V. Vaskonen, *JHEP* **06**, 075 (2019), [arXiv:1904.01329 \[hep-ph\]](#).
- [75] A. Paul, U. Mukhopadhyay, and D. Majumdar, *JHEP* **05**, 223 (2021), [arXiv:2010.03439 \[hep-ph\]](#).
- [76] W. Su, A. G. Williams, and M. Zhang, *JHEP* **04**, 219 (2021), [arXiv:2011.04540 \[hep-ph\]](#).
- [77] R. Apreda, M. Maggiore, A. Nicolis, and A. Riotto, *Nucl. Phys. B* **631**, 342 (2002), [arXiv:gr-qc/0107033](#).
- [78] S. J. Huber, T. Konstandin, G. Nardini, and I. Rues, *JCAP* **03**, 036 (2016), [arXiv:1512.06357 \[hep-ph\]](#).
- [79] S. J. Huber and T. Konstandin, *JCAP* **05**, 017 (2008), [arXiv:0709.2091 \[hep-ph\]](#).
- [80] S. V. Demidov, D. S. Gorbunov, and D. V. Kirpichnikov, *Phys. Lett. B* **779**, 191 (2018), [arXiv:1712.00087 \[hep-ph\]](#).
- [81] V. Brdar, L. Graf, A. J. Helmboldt, and X.-J. Xu, *JCAP* **12**, 027 (2019), [arXiv:1909.02018 \[hep-ph\]](#).
- [82] M. Li, Q.-S. Yan, Y. Zhang, and Z. Zhao, *JHEP* **03**, 267 (2021), [arXiv:2012.13686 \[hep-ph\]](#).
- [83] W.-C. Huang, F. Sannino, and Z.-W. Wang, *Phys. Rev. D* **102**, 095025 (2020), [arXiv:2004.02332 \[hep-ph\]](#).
- [84] C.-W. Chiang and T. Yamada, *Phys. Lett. B* **735**, 295 (2014), [arXiv:1404.5182 \[hep-ph\]](#).
- [85] V. Q. Phong, N. C. Thao, and H. N. Long, *Phys. Rev. D* **97**, 115008 (2018), [arXiv:1511.00579 \[hep-ph\]](#).
- [86] V. Q. Phong, N. C. Thao, and H. N. Long, *Eur. Phys. J. C* **82**, 1005 (2022), [arXiv:2107.13823 \[hep-ph\]](#).
- [87] J. R. Espinosa, B. Gripaios, T. Konstandin, and F. Riva, *JCAP* **01**, 012 (2012), [arXiv:1110.2876 \[hep-ph\]](#).
- [88] M. Chala, G. Nardini, and I. Sobolev, *Phys. Rev. D* **94**, 055006 (2016),

- [arXiv:1605.08663 \[hep-ph\]](#).
- [89] S. Bruggisser, B. Von Harling, O. Matsedonskyi, and G. Servant, *Phys. Rev. Lett.* **121**, 131801 (2018), [arXiv:1803.08546 \[hep-ph\]](#).
 - [90] S. Bruggisser, B. Von Harling, O. Matsedonskyi, and G. Servant, *JHEP* **12**, 099 (2018), [arXiv:1804.07314 \[hep-ph\]](#).
 - [91] L. Bian, Y. Wu, and K.-P. Xie, *JHEP* **12**, 028 (2019), [arXiv:1909.02014 \[hep-ph\]](#).
 - [92] S. De Curtis, L. Delle Rose, and G. Panico, *JHEP* **12**, 149 (2019), [arXiv:1909.07894 \[hep-ph\]](#).
 - [93] K.-P. Xie, L. Bian, and Y. Wu, *JHEP* **12**, 047 (2020), [arXiv:2005.13552 \[hep-ph\]](#).
 - [94] P. Di Bari, D. Marfatia, and Y.-L. Zhou, *JHEP* **10**, 193 (2021), [arXiv:2106.00025 \[hep-ph\]](#).
 - [95] R. Zhou, L. Bian, and Y. Du, *JHEP* **08**, 205 (2022), [arXiv:2203.01561 \[hep-ph\]](#).
 - [96] P. Schwaller, *Phys. Rev. Lett.* **115**, 181101 (2015), [arXiv:1504.07263 \[hep-ph\]](#).
 - [97] I. Baldes and C. Garcia-Cely, *JHEP* **05**, 190 (2019), [arXiv:1809.01198 \[hep-ph\]](#).
 - [98] M. Breitbach, J. Kopp, E. Madge, T. Opferkuch, and P. Schwaller, *JCAP* **07**, 007 (2019), [arXiv:1811.11175 \[hep-ph\]](#).
 - [99] D. Croon, V. Sanz, and G. White, *JHEP* **08**, 203 (2018), [arXiv:1806.02332 \[hep-ph\]](#).
 - [100] I. Baldes, *JCAP* **05**, 028 (2017), [arXiv:1702.02117 \[hep-ph\]](#).
 - [101] D. Croon, A. Kusenko, A. Mazumdar, and G. White, *Phys. Rev. D* **101**, 085010 (2020), [arXiv:1910.09562 \[hep-ph\]](#).
 - [102] E. Hall, T. Konstandin, R. McGehee, and H. Murayama, *Phys. Rev. D* **107**, 055011 (2023), [arXiv:1911.12342 \[hep-ph\]](#).
 - [103] E. Hall, T. Konstandin, R. McGehee, H. Murayama, and G. Servant, *JHEP* **04**, 042 (2020), [arXiv:1910.08068 \[hep-ph\]](#).
 - [104] W. Chao, X.-F. Li, and L. Wang, *JCAP* **06**, 038 (2021), [arXiv:2012.15113 \[hep-ph\]](#).
 - [105] J. B. Dent, B. Dutta, S. Ghosh, J. Kumar, and J. Runburg, *JHEP* **08**, 300 (2022),

- [arXiv:2203.11736 \[hep-ph\]](#).
- [106] S. Weinberg, *Phys. Rev. D* **9**, 3357 (1974).
- [107] D. Land and E. D. Carlson, *Phys. Lett. B* **292**, 107 (1992), [arXiv:hep-ph/9208227](#).
- [108] H. H. Patel and M. J. Ramsey-Musolf, *Phys. Rev. D* **88**, 035013 (2013), [arXiv:1212.5652 \[hep-ph\]](#).
- [109] H. H. Patel, M. J. Ramsey-Musolf, and M. B. Wise, *Phys. Rev. D* **88**, 015003 (2013), [arXiv:1303.1140 \[hep-ph\]](#).
- [110] N. Blinov, J. Kozaczuk, D. E. Morrissey, and C. Tamarit, *Phys. Rev. D* **92**, 035012 (2015), [arXiv:1504.05195 \[hep-ph\]](#).
- [111] D. Croon and G. White, *JHEP* **05**, 210 (2018), [arXiv:1803.05438 \[hep-ph\]](#).
- [112] A. P. Morais, R. Pasechnik, and T. Vieu, *PoS EPS-HEP2019*, 054 (2020), [arXiv:1802.10109 \[hep-ph\]](#).
- [113] A. P. Morais and R. Pasechnik, *JCAP* **04**, 036 (2020), [arXiv:1910.00717 \[hep-ph\]](#).
- [114] A. Angelescu and P. Huang, *Phys. Rev. D* **99**, 055023 (2019), [arXiv:1812.08293 \[hep-ph\]](#).
- [115] L. S. Friedrich, M. J. Ramsey-Musolf, T. V. I. Tenkanen, and V. Q. Tran, (2022), [arXiv:2203.05889 \[hep-ph\]](#).
- [116] A. D. Sakharov, *Pisma Zh. Eksp. Teor. Fiz.* **5**, 32 (1967).
- [117] M. Trodden, *Rev. Mod. Phys.* **71**, 1463 (1999), [arXiv:hep-ph/9803479](#).
- [118] J. M. Cline, in *Les Houches Summer School - Session 86: Particle Physics and Cosmology: The Fabric of the Universe* (2006) [arXiv:hep-ph/0609145](#).
- [119] D. E. Morrissey and M. J. Ramsey-Musolf, *New J. Phys.* **14**, 125003 (2012), [arXiv:1206.2942 \[hep-ph\]](#).
- [120] G. A. White, (2016), [10.1088/978-1-6817-4457-5](#).
- [121] B. Garbrecht, *Prog. Part. Nucl. Phys.* **110**, 103727 (2020), [arXiv:1812.02651 \[hep-ph\]](#).
- [122] M. J. Ramsey-Musolf, *JHEP* **09**, 179 (2020), [arXiv:1912.07189 \[hep-ph\]](#).

- [123] M. Carena, J. Kozaczuk, Z. Liu, T. Ou, M. J. Ramsey-Musolf, J. Shelton, Y. Wang, and K.-P. Xie, *LHEP* **2023**, 432 (2023), [arXiv:2203.08206 \[hep-ph\]](#).
- [124] Z. Wang, X. Zhu, E. E. Khoda, S.-C. Hsu, N. Konstantinidis, K. Li, S. Li, M. J. Ramsey-Musolf, Y. Wu, and Y. E. Zhang, in *Snowmass 2021* (2022) [arXiv:2203.10184 \[hep-ex\]](#).
- [125] W. Zhang, H.-L. Li, K. Liu, M. J. Ramsey-Musolf, Y. Zeng, and S. Arunasalam, *JHEP* **12**, 018 (2023), [arXiv:2303.03612 \[hep-ph\]](#).
- [126] Z. Wang, X. Zhu, E. E. Khoda, S.-C. Hsu, N. Konstantinidis, K. Li, S. Li, M. J. Ramsey-Musolf, Y. Wu, and Y. E. Zhang, *LHEP* **2023**, 436 (2023).
- [127] T. A. Chowdhury, M. Nemevsek, G. Senjanovic, and Y. Zhang, *JCAP* **02**, 029 (2012), [arXiv:1110.5334 \[hep-ph\]](#).
- [128] A. Katz, M. Perelstein, M. J. Ramsey-Musolf, and P. Winslow, *Phys. Rev. D* **92**, 095019 (2015), [arXiv:1509.02934 \[hep-ph\]](#).
- [129] S. Fabian, F. Goertz, and Y. Jiang, *JCAP* **09**, 011 (2021), [arXiv:2012.12847 \[hep-ph\]](#).
- [130] N. F. Bell, M. J. Dolan, L. S. Friedrich, M. J. Ramsey-Musolf, and R. R. Volkas, *JHEP* **05**, 050 (2020), [arXiv:2001.05335 \[hep-ph\]](#).
- [131] C.-W. Chiang, D. Huang, and B.-Q. Lu, *JCAP* **01**, 035 (2021), [arXiv:2009.08635 \[hep-ph\]](#).
- [132] W. Zhang, Y. Cai, M. J. Ramsey-Musolf, and L. Zhang, *JHEP* **01**, 051 (2024), [arXiv:2307.01615 \[hep-ph\]](#).
- [133] D. J. Weir, *Phil. Trans. Roy. Soc. Lond. A* **376**, 20170126 (2018), [arXiv:1705.01783 \[hep-ph\]](#).
- [134] P. Amaro-Seoane et al. (LISA), (2017), [arXiv:1702.00786 \[astro-ph.IM\]](#).
- [135] T. Robson, N. J. Cornish, and C. Liu, *Class. Quant. Grav.* **36**, 105011 (2019), [arXiv:1803.01944 \[astro-ph.HE\]](#).
- [136] J. Crowder and N. J. Cornish, *Phys. Rev. D* **72**, 083005 (2005), [arXiv:gr-](#)

qc/0506015.

- [137] J. Luo et al. (TianQin), *Class. Quant. Grav.* **33**, 035010 (2016), [arXiv:1512.02076 \[astro-ph.IM\]](#).
- [138] Y.-M. Hu, J. Mei, and J. Luo, *Natl. Sci. Rev.* **4**, 683 (2017).
- [139] W.-R. Hu and Y.-L. Wu, *Natl. Sci. Rev.* **4**, 685 (2017).
- [140] W.-H. Ruan, Z.-K. Guo, R.-G. Cai, and Y.-Z. Zhang, *Int. J. Mod. Phys. A* **35**, 2050075 (2020), [arXiv:1807.09495 \[gr-qc\]](#).
- [141] S. Kawamura et al., *Class. Quant. Grav.* **23**, S125 (2006).
- [142] S. Kawamura et al., *Class. Quant. Grav.* **28**, 094011 (2011).
- [143] M. Musha (DECIGO Working group), *Proc. SPIE Int. Soc. Opt. Eng.* **10562**, 105623T (2017).
- [144] P. Ghorbani, *Phys. Dark Univ.* **33**, 100861 (2021), [arXiv:2010.15708 \[hep-ph\]](#).
- [145] H. H. Patel and M. J. Ramsey-Musolf, *JHEP* **07**, 029 (2011), [arXiv:1101.4665 \[hep-ph\]](#).
- [146] R. Ramos, V. Q. Tran, and T.-C. Yuan, *JHEP* **11**, 112 (2021), [arXiv:2109.03185 \[hep-ph\]](#).
- [147] R. Ramos, V. Q. Tran, and T.-C. Yuan, *Phys. Rev. D* **103**, 075021 (2021), [arXiv:2101.07115 \[hep-ph\]](#).
- [148] W.-C. Huang, Y.-L. S. Tsai, and T.-C. Yuan, *JHEP* **04**, 019 (2016), [arXiv:1512.00229 \[hep-ph\]](#).
- [149] C.-R. Chen, Y.-X. Lin, C. S. Nugroho, R. Ramos, Y.-L. S. Tsai, and T.-C. Yuan, *Phys. Rev. D* **101**, 035037 (2020), [arXiv:1910.13138 \[hep-ph\]](#).
- [150] V. Q. Tran and T.-C. Yuan, *JHEP* **02**, 117 (2023), [arXiv:2212.02333 \[hep-ph\]](#).
- [151] C. H. Liu, V. Q. Tran, Q. Wen, F. Xu, and T.-C. Yuan, (2024), [arXiv:2404.06397 \[hep-ph\]](#).
- [152] V. Q. Tran, T. T. Q. Nguyen, and T.-C. Yuan, *Eur. Phys. J. C* **83**, 346 (2023), [arXiv:2208.10971 \[hep-ph\]](#).

- [153] W.-C. Huang, Y.-L. S. Tsai, and T.-C. Yuan, *Nucl. Phys. B* **909**, 122 (2016), [arXiv:1512.07268 \[hep-ph\]](#).
- [154] A. Arhrib, W.-C. Huang, R. Ramos, Y.-L. S. Tsai, and T.-C. Yuan, *Phys. Rev. D* **98**, 095006 (2018), [arXiv:1806.05632 \[hep-ph\]](#).
- [155] C.-T. Huang, R. Ramos, V. Q. Tran, Y.-L. S. Tsai, and T.-C. Yuan, *JHEP* **09**, 048 (2019), [arXiv:1905.02396 \[hep-ph\]](#).
- [156] W.-C. Huang, H. Ishida, C.-T. Lu, Y.-L. S. Tsai, and T.-C. Yuan, *Eur. Phys. J. C* **78**, 613 (2018), [arXiv:1708.02355 \[hep-ph\]](#).
- [157] C.-R. Chen, Y.-X. Lin, V. Q. Tran, and T.-C. Yuan, *Phys. Rev. D* **99**, 075027 (2019), [arXiv:1810.04837 \[hep-ph\]](#).
- [158] B. Dirgantara and C. S. Nugroho, *Eur. Phys. J. C* **82**, 142 (2022), [arXiv:2012.13170 \[hep-ph\]](#).
- [159] V. Q. Tran, T. T. Q. Nguyen, and T.-C. Yuan, *JCAP* **05**, 015 (2024), [arXiv:2312.10785 \[hep-ph\]](#).
- [160] A. M. Sirunyan et al. (CMS), *Phys. Lett. B* **805**, 135425 (2020), [arXiv:2002.06398 \[hep-ex\]](#).
- [161] P. A. Zyla et al. (Particle Data Group), *PTEP* **2020**, 083C01 (2020).
- [162] CMS-Collaboration (CMS), (2020), [CMS-PAS-HIG-19-005](#).
- [163] (2021).
- [164] A. Tumasyan et al. (CMS), *Phys. Rev. D* **105**, 092007 (2022), [arXiv:2201.11585 \[hep-ex\]](#).
- [165] G. Aad et al. (ATLAS), *Phys. Lett. B* **796**, 68 (2019), [arXiv:1903.06248 \[hep-ex\]](#).
- [166] M. Fabbrichesi, E. Gabrielli, and G. Lanfranchi, (2020), [10.1007/978-3-030-62519-1](#), [arXiv:2005.01515 \[hep-ph\]](#).
- [167] T. Aaltonen et al. (CDF), *Science* **376**, 170 (2022).
- [168] N. Aghanim et al. (Planck), *Astron. Astrophys.* **641**, A6 (2020), [Erratum: *Astron. Astrophys.* 652, C4 (2021)], [arXiv:1807.06209 \[astro-ph.CO\]](#).

- [169] G. Bélanger, F. Boudjema, A. Goudelis, A. Pukhov, and B. Zaldivar, *Comput. Phys. Commun.* **231**, 173 (2018), [arXiv:1801.03509 \[hep-ph\]](#).
- [170] G. Angloher *et al.* (CRESST), *Eur. Phys. J. C* **77**, 637 (2017), [arXiv:1707.06749 \[astro-ph.CO\]](#).
- [171] P. Agnes *et al.* (DarkSide), *Phys. Rev. Lett.* **121**, 081307 (2018), [arXiv:1802.06994 \[astro-ph.HE\]](#).
- [172] P. Agnes *et al.* (DarkSide-50), *Phys. Rev. D* **107**, 063001 (2023), [arXiv:2207.11966 \[hep-ex\]](#).
- [173] E. Aprile *et al.* (XENON), *Phys. Rev. Lett.* **121**, 111302 (2018), [arXiv:1805.12562 \[astro-ph.CO\]](#).
- [174] E. Aprile *et al.* (XENON), *Phys. Rev. Lett.* **123**, 251801 (2019), [arXiv:1907.11485 \[hep-ex\]](#).
- [175] E. Aprile *et al.* (XENON), *Phys. Rev. Lett.* **131**, 041003 (2023), [arXiv:2303.14729 \[hep-ex\]](#).
- [176] Y. Meng *et al.* (PandaX-4T), *Phys. Rev. Lett.* **127**, 261802 (2021), [arXiv:2107.13438 \[hep-ex\]](#).
- [177] J. Aalbers *et al.* (LZ), *Phys. Rev. Lett.* **131**, 041002 (2023), [arXiv:2207.03764 \[hep-ex\]](#).
- [178] M. Ackermann *et al.* (Fermi-LAT), *Phys. Rev. Lett.* **115**, 231301 (2015), [arXiv:1503.02641 \[astro-ph.HE\]](#).
- [179] A. Albert *et al.* (Fermi-LAT, DES), *Astrophys. J.* **834**, 110 (2017), [arXiv:1611.03184 \[astro-ph.HE\]](#).
- [180] A. D. Linde, *Phys. Lett. B* **96**, 289 (1980).
- [181] P. B. Arnold, *Phys. Rev. D* **46**, 2628 (1992), [arXiv:hep-ph/9204228](#).
- [182] R. R. Parwani, *Phys. Rev. D* **45**, 4695 (1992), [Erratum: *Phys.Rev.D* 48, 5965 (1993)], [arXiv:hep-ph/9204216](#).
- [183] D. Curtin, P. Meade, and H. Ramani, *Eur. Phys. J. C* **78**, 787 (2018),

- arXiv:1612.00466 [hep-ph].
- [184] D. Curtin, J. Roy, and G. White, *Phys. Rev. D* **109**, 116001 (2024), arXiv:2211.08218 [hep-ph].
- [185] C. Wainwright, S. Profumo, and M. J. Ramsey-Musolf, *Phys. Rev. D* **84**, 023521 (2011), arXiv:1104.5487 [hep-ph].
- [186] M. Laine, *Phys. Rev. D* **51**, 4525 (1995), arXiv:hep-ph/9411252.
- [187] N. K. Nielsen, *Nucl. Phys. B* **101**, 173 (1975).
- [188] R. Fukuda and T. Kugo, *Phys. Rev. D* **13**, 3469 (1976).
- [189] D. Croon, O. Gould, P. Schicho, T. V. I. Tenkanen, and G. White, *JHEP* **04**, 055 (2021), arXiv:2009.10080 [hep-ph].
- [190] O. Gould and T. V. I. Tenkanen, *JHEP* **06**, 069 (2021), arXiv:2104.04399 [hep-ph].
- [191] P. Athron, C. Balazs, A. Fowlie, L. Morris, G. White, and Y. Zhang, *JHEP* **01**, 050 (2023), arXiv:2208.01319 [hep-ph].
- [192] K. Kajantie, M. Laine, K. Rummukainen, and M. E. Shaposhnikov, *Nucl. Phys. B* **458**, 90 (1996), arXiv:hep-ph/9508379.
- [193] K. Farakos, K. Kajantie, K. Rummukainen, and M. E. Shaposhnikov, *Nucl. Phys. B* **442**, 317 (1995), arXiv:hep-lat/9412091.
- [194] A. Ekstedt, P. Schicho, and T. V. I. Tenkanen, *Comput. Phys. Commun.* **288**, 108725 (2023), arXiv:2205.08815 [hep-ph].
- [195] L. Niemi, P. Schicho, and T. V. I. Tenkanen, *Phys. Rev. D* **103**, 115035 (2021), arXiv:2103.07467 [hep-ph].
- [196] P. Schicho, T. V. I. Tenkanen, and G. White, *JHEP* **11**, 047 (2022), arXiv:2203.04284 [hep-ph].
- [197] A. Ekstedt and J. Löfgren, *JHEP* **12**, 136 (2020), arXiv:2006.12614 [hep-ph].
- [198] L. Niemi, M. J. Ramsey-Musolf, T. V. I. Tenkanen, and D. J. Weir, *Phys. Rev. Lett.* **126**, 171802 (2021), arXiv:2005.11332 [hep-ph].
- [199] O. Gould, S. Güyer, and K. Rummukainen, *Phys. Rev. D* **106**, 114507 (2022),

- [arXiv:2205.07238 \[hep-lat\]](#).
- [200] L. Niemi, M. J. Ramsey-Musolf, and G. Xia, (2024), [arXiv:2405.01191 \[hep-ph\]](#).
- [201] S. R. Coleman and E. J. Weinberg, *Phys. Rev. D* **7**, 1888 (1973).
- [202] E. J. Weinberg, Radiative corrections as the origin of spontaneous symmetry breaking, Ph.D. thesis, Harvard U. (1973), [arXiv:hep-th/0507214](#).
- [203] L. Dolan and R. Jackiw, *Phys. Rev. D* **9**, 3320 (1974).
- [204] P. B. Arnold and O. Espinosa, *Phys. Rev. D* **47**, 3546 (1993), [Erratum: *Phys.Rev.D* 50, 6662 (1994)], [arXiv:hep-ph/9212235](#).
- [205] M. E. Carrington, *Phys. Rev. D* **45**, 2933 (1992).
- [206] P. Athron, C. Balázs, A. Fowlie, and Y. Zhang, *Eur. Phys. J. C* **80**, 567 (2020), [arXiv:2003.02859 \[hep-ph\]](#).
- [207] R. N. Mohapatra and G. Senjanovic, *Phys. Rev. D* **20**, 3390 (1979).
- [208] A. Masiero, D. V. Nanopoulos, and T. Yanagida, *Phys. Lett. B* **138**, 91 (1984).
- [209] P. Salomonson and B.-S. K. Skagerstam, *Phys. Lett. B* **155**, 100 (1985).
- [210] T. W. Kephart, T. J. Weiler, and T. C. Yuan, *Nucl. Phys. B* **330**, 705 (1990).
- [211] P. Langacker and S.-Y. Pi, *Phys. Rev. Lett.* **45**, 1 (1980).
- [212] T. H. Farris, T. W. Kephart, T. J. Weiler, and T. C. Yuan, *Phys. Rev. Lett.* **68**, 564 (1992).
- [213] D. Foreman-Mackey, D. W. Hogg, D. Lang, and J. Goodman, *Publ. Astron. Soc. Pac.* **125**, 306 (2013), [arXiv:1202.3665 \[astro-ph.IM\]](#).
- [214] P. A. Zyla *et al.* (Particle Data Group), *PTEP* **2020**, 083C01 (2020).
- [215] C. Caprini *et al.*, *JCAP* **04**, 001 (2016), [arXiv:1512.06239 \[astro-ph.CO\]](#).
- [216] R. Jinno and M. Takimoto, *Phys. Rev. D* **95**, 024009 (2017), [arXiv:1605.01403 \[astro-ph.CO\]](#).
- [217] A. Kosowsky, M. S. Turner, and R. Watkins, *Phys. Rev. D* **45**, 4514 (1992).
- [218] A. Kosowsky, M. S. Turner, and R. Watkins, *Phys. Rev. Lett.* **69**, 2026 (1992).
- [219] A. Kosowsky and M. S. Turner, *Phys. Rev. D* **47**, 4372 (1993), [arXiv:astro-](#)

- ph/9211004.
- [220] S. J. Huber and T. Konstandin, *JCAP* **09**, 022 (2008), [arXiv:0806.1828 \[hep-ph\]](#).
 - [221] M. Hindmarsh, S. J. Huber, K. Rummukainen, and D. J. Weir, *Phys. Rev. Lett.* **112**, 041301 (2014), [arXiv:1304.2433 \[hep-ph\]](#).
 - [222] J. T. Giblin, Jr. and J. B. Mertens, *JHEP* **12**, 042 (2013), [arXiv:1310.2948 \[hep-th\]](#).
 - [223] J. T. Giblin and J. B. Mertens, *Phys. Rev. D* **90**, 023532 (2014), [arXiv:1405.4005 \[astro-ph.CO\]](#).
 - [224] M. Hindmarsh, S. J. Huber, K. Rummukainen, and D. J. Weir, *Phys. Rev. D* **92**, 123009 (2015), [arXiv:1504.03291 \[astro-ph.CO\]](#).
 - [225] M. Hindmarsh, S. J. Huber, K. Rummukainen, and D. J. Weir, *Phys. Rev. D* **96**, 103520 (2017), [Erratum: *Phys.Rev.D* 101, 089902 (2020)], [arXiv:1704.05871 \[astro-ph.CO\]](#).
 - [226] D. Cutting, M. Hindmarsh, and D. J. Weir, *Phys. Rev. Lett.* **125**, 021302 (2020), [arXiv:1906.00480 \[hep-ph\]](#).
 - [227] M. Hindmarsh, *Phys. Rev. Lett.* **120**, 071301 (2018), [arXiv:1608.04735 \[astro-ph.CO\]](#).
 - [228] M. Hindmarsh and M. Hijazi, *JCAP* **12**, 062 (2019), [arXiv:1909.10040 \[astro-ph.CO\]](#).
 - [229] C. Caprini and R. Durrer, *Phys. Rev. D* **74**, 063521 (2006), [arXiv:astro-ph/0603476](#).
 - [230] T. Kahniashvili, A. Kosowsky, G. Gogoberidze, and Y. Maravin, *Phys. Rev. D* **78**, 043003 (2008), [arXiv:0806.0293 \[astro-ph\]](#).
 - [231] T. Kahniashvili, L. Campanelli, G. Gogoberidze, Y. Maravin, and B. Ratra, *Phys. Rev. D* **78**, 123006 (2008), [Erratum: *Phys.Rev.D* 79, 109901 (2009)], [arXiv:0809.1899 \[astro-ph\]](#).
 - [232] T. Kahniashvili, L. Kisslinger, and T. Stevens, *Phys. Rev. D* **81**, 023004 (2010), [arXiv:0905.0643 \[astro-ph.CO\]](#).

- [233] C. Caprini, R. Durrer, and G. Servant, *JCAP* **12**, 024 (2009), [arXiv:0909.0622 \[astro-ph.CO\]](#).
- [234] M. B. Hindmarsh, M. Lüben, J. Lumma, and M. Pauly, *SciPost Phys. Lect. Notes* **24**, 1 (2021), [arXiv:2008.09136 \[astro-ph.CO\]](#).
- [235] P. Athron, C. Balázs, A. Fowlie, L. Morris, and L. Wu, *Prog. Part. Nucl. Phys.* **135**, 104094 (2024), [arXiv:2305.02357 \[hep-ph\]](#).
- [236] C. L. Wainwright, *Comput. Phys. Commun.* **183**, 2006 (2012), [arXiv:1109.4189 \[hep-ph\]](#).
- [237] C. Caprini *et al.*, *JCAP* **03**, 024 (2020), [arXiv:1910.13125 \[astro-ph.CO\]](#).
- [238] D. Durnford and M.-C. Piro (NEWS-G), *J. Phys. Conf. Ser.* **2156**, 012059 (2021), [arXiv:2111.02796 \[physics.ins-det\]](#).
- [239] R. Agnese *et al.* (SuperCDMS), *Phys. Rev. D* **95**, 082002 (2017), [arXiv:1610.00006 \[physics.ins-det\]](#).
- [240] H. Ma *et al.* (CDEX), *J. Phys. Conf. Ser.* **1342**, 012067 (2020), [arXiv:1712.06046 \[hep-ex\]](#).
- [241] S. A. Hertel, A. Biekert, J. Lin, V. Velan, and D. N. McKinsey, *Phys. Rev. D* **100**, 092007 (2019), [arXiv:1810.06283 \[physics.ins-det\]](#).
- [242] X. Wang, Z. Lei, Y. Ju, J. Liu, N. Zhou, Y. Chen, Z. Wang, X. Cui, Y. Meng, and L. Zhao, *JINST* **18**, P05028 (2023), [arXiv:2301.06044 \[physics.ins-det\]](#).
- [243] E. Aprile *et al.* (XENON), *JCAP* **11**, 031 (2020), [arXiv:2007.08796 \[physics.ins-det\]](#).
- [244] C. E. Aalseth *et al.* (DarkSide-20k), *Eur. Phys. J. Plus* **133**, 131 (2018), [arXiv:1707.08145 \[physics.ins-det\]](#).
- [245] J. Aalbers *et al.* (DARWIN), *JCAP* **11**, 017 (2016), [arXiv:1606.07001 \[astro-ph.IM\]](#).
- [246] R. Essig, G. K. Giovanetti, N. Kurinsky, D. McKinsey, K. Ramanathan, K. Stifter, and T.-T. Yu, in *2022 Snowmass Summer Study* (2022) [arXiv:2203.08297 \[hep-ph\]](#).
- [247] M. Quiros, in *ICTP Summer School in High-Energy Physics and Cosmology*

- (1999) pp. 187–259, [arXiv:hep-ph/9901312](#).
- [248] G. W. Anderson and L. J. Hall, *Phys. Rev. D* **45**, 2685 (1992).
- [249] J. R. Espinosa, *Nucl. Phys. B* **475**, 273 (1996), [arXiv:hep-ph/9604320](#).
- [250] B. M. Kastening, *Phys. Lett. B* **283**, 287 (1992).
- [251] M. Bando, T. Kugo, N. Maekawa, and H. Nakano, *Phys. Lett. B* **301**, 83 (1993), [arXiv:hep-ph/9210228](#).
- [252] C. Ford, D. R. T. Jones, P. W. Stephenson, and M. B. Einhorn, *Nucl. Phys. B* **395**, 17 (1993), [arXiv:hep-lat/9210033](#).
- [253] K. Funakubo and E. Senaha, *Phys. Rev. D* **109**, L071901 (2024), [arXiv:2307.02153](#) [hep-ph].
- [254] K. Funakubo and E. Senaha, *Phys. Rev. D* **109**, 056023 (2024), [arXiv:2308.15876](#) [hep-ph].
- [255] F. Staub, *Comput. Phys. Commun.* **185**, 1773 (2014), [arXiv:1309.7223](#) [hep-ph].